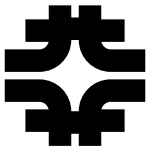

Fermi National Accelerator Laboratory

FERMILAB-FN-640

The Standard Model and Beyond: Physics with the D0 Experiment

Paul Quintas et al., ed.

For the D0 Collaboration

Fermi National Accelerator Laboratory
P.O. Box 500, Batavia, Illinois 60510

February 1996

Operated by Universities Research Association Inc. under Contract No. DE-AC02-76CHO3000 with the United States Department of Energy

Disclaimer

The Standard Model and Beyond: Physics with the DØ Experiment

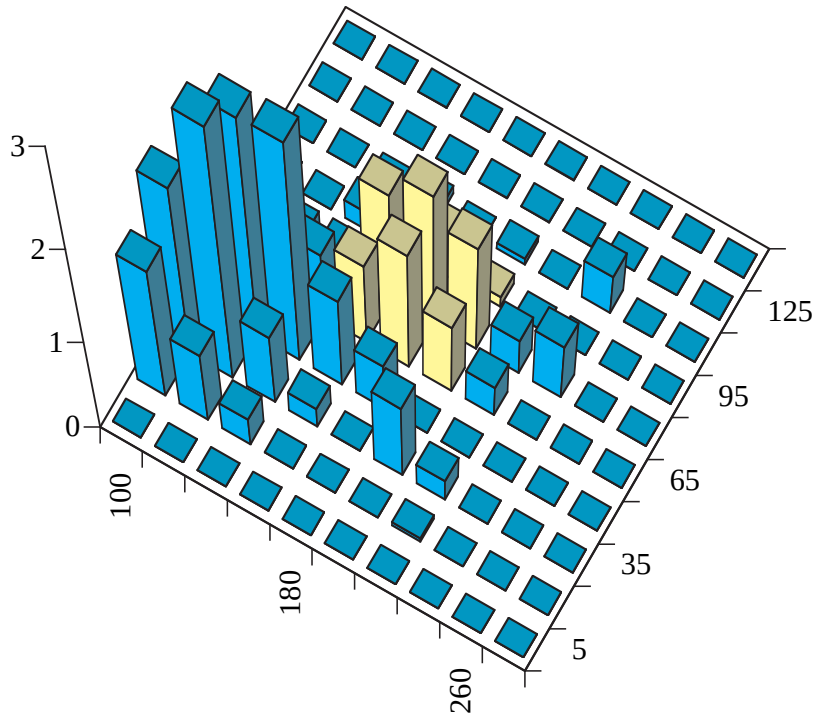

Editor: Paul Quintas
Contributors: Stefan Gruenendahl, Terry Heuring, Thorsten Huehn,
Greg Landsberg, Lee Sawyer, Gordon Watts
December 15, 1995

Contents

1 Introduction

The DØ detector was designed and constructed over the period 1983–1992 and rolled into the collision hall at the Fermilab Tevatron on February 14, 1992. Since then data has been collected from an integrated luminosity of 14 pb^{-1} during 1992–93 and a further 85 pb^{-1} during 1994-95. This document gives an overview of results to date from the experiment. These are cast within the framework of the current $SU(3)_c \times SU(2)_L \times U(1)_Y$ standard model (SM) of elementary particles and their interactions. In this model the $SU(3)_c$ describes the strong interactions based upon the three color degrees of freedom (quantum chromodynamics or QCD) and the $SU(2)_L \times U(1)_Y$ describes the unified electroweak interaction in which the underlying gauge bosons and fermions transform according to the $SU(2)_L$ symmetry of weak isospin and the $U(1)_Y$ symmetry of weak hypercharge. In addition, the DØ data begin to test sensitively some models of physics beyond the SM, for instance those incorporating supersymmetry, such as the Minimal Supersymmetric Standard Model.

The DØ detector, shown in Fig. 1, is designed to identify and measure the fundamental particles of the standard model. It consists of a compact tracking volume containing drift chambers and a transition radiation detector encapsulated in a hermetic depleted-uranium calorimeter using liquid argon as the sensitive sampling medium. The whole is surrounded by an extensive muon detection and momentum measurement system of toroids and proportional drift tubes. The stable charged leptons, the electrons (e) and muons (μ), are fully measured in the calorimeter and muon system respectively. Neutral leptons, the neutrinos (ν), are inferred from the measurement of the transverse energy imbalance in events. Light quarks (up (u), down (d) and strange (s)) are detected as jets in the calorimeter. The heavy quarks (charm (c) and bottom (b)) are signaled by a muon or electron accompanying a jet as the heavy quark undergoes semi-leptonic decay. The heaviest quark, the top (t), is a primary focus of our research and is detected through its characteristic decays into other objects. The intermediate bosons of the strong interaction, the gluons (g), have a similar signature to that of light quarks. The intermediate boson of the electromagnetic interaction, the photon (γ), gives a similar signal to that of the electron except that there is no associated charged particle track. The remaining electroweak bosons, the $W^{\pm}$ and Z, are detected through their leptonic decays.

One of the most basic tests of a physical model is the observation of all the predicted states. The u, d, s, c and b quarks have been with us since since 1977, but the sixth, demanded by the SM, had eluded discovery for many years. In Section 2, we describe the observation of that quark, *the top*.

The strong interaction is mediated by a set of eight colored gluons, exchanged between the color-carrying quarks (of any flavor) or other gluons. In principle, QCD theory describes all aspects of the strong interactions, though in practice calculation is difficult and experiment is needed to guide and refine the theory. There are many ways to investigate this interaction. In Section 3, we describe our measurements of the parton distributions within the proton, and the basic interactions as observed through gluons and light quarks, the heavy quarks, and the bosons γ, W, and Z. Finally, we discuss several modern QCD studies which are sensitive to gluon interference effects.

The electroweak interactions have been investigated through study of the properties of the W and Z bosons. The mass of the top quark is so large that it produces finite electroweak

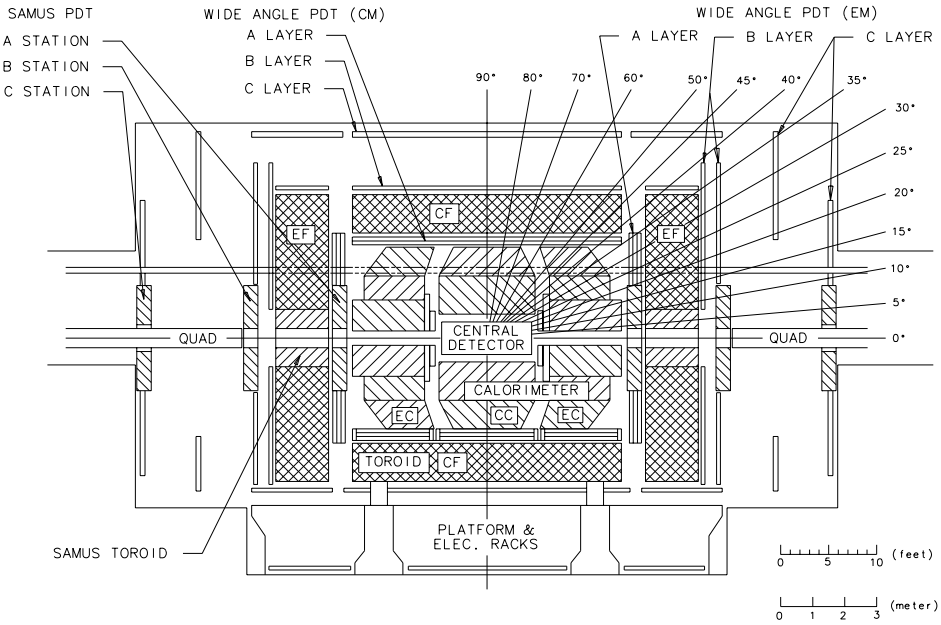

Figure 1: The DØ Detector in a side view showing the location of the component systems.

radiative corrections, and thus in a practical sense it also is a parameter of the electroweak standard model. The precision measurements of the electroweak model parameters and the way that they may point to the Higgs particle, the mysterious "giver of mass" in the standard model, are described in Section 4.

The standard model is confined to a prescription of a mechanism by which the electroweak symmetry breaking can be generated, but makes no prediction of the detailed implementation. A driving principle in physics is that "unification is good" and many have imagined a unification of all the forces of nature. This could happen if all the coupling strengths were to evolve to a common value at some high scale, where Grand Unification of the forces would occur. The current ideas suggest that this is in the range 10^{15} GeV for the strong and electroweak interactions. However, in this context, the standard model doesn't quite work, or is unsatisfactory, for several reasons. An intermediate-scale supersymmetry relating fermions and bosons and predicting an approximate doubling of the fundamental particles has been suggested as a solution. The search for supersymmetric particles, or for evidence of other extensions beyond the standard model (or indeed beyond any explicit model), is described in Section 5.

The primary goal of this review is to describe the results obtained thus far by the DØ experiment. However there are well-advanced plans for enhancements to the detector which will permit it to extend its physics reach by exploiting the higher collision rates of an upgraded Tevatron. These will arise with the completion of the Main Injector, the feeder accelerator and source of antiprotons for the collisions in the Tevatron. It is expected that luminosities in the range 2×10^{32} cm^{-2}s^{-1} will be achieved. The potential of the approved upgraded DØ detector will be described in Section 6.

Finally, in Section 7, we make some concluding remarks.

2 Top Physics

The standard model provides a classification scheme for the fermions, and a prescription for their interaction. Before 1977, there were four known quarks grouped together in two isospin doublets. The discovery of the bottom quark in 1977 and the subsequent determination that its isospin is $-\frac{1}{2}$ were compelling reasons to believe in the existence of a sixth quark, the top. Searches for this quark, however, were unsuccessful until its observation by DØ and CDF in early 1995.

The measured mass of the top quark is anomalously high: it is about 40 times more massive than the next heaviest quark, the bottom quark. Thus, understanding top quark physics is even more imperative than was the search for its existence. In the SM, the Higgs boson breaks the $SU(2)_L \times U(1)_Y$ symmetry and also gives masses to the fermions. This mechanism for the generation of the fermion masses is particularly unappealing as it introduces one new parameter for each fermion. It is hoped that study of the top quark can give clues about the fundamental origin of mass since, whatever the origin of electroweak symmetry breaking, the top quark is most strongly coupled to the mass-generating sector.

2.1 Searches for the Top Quark

In March, 1995, DØ and CDF jointly announced the discovery of the top quark. This ended a search, started over 15 years ago with the discovery of the bottom quark, conducted in many experiments at accelerators throughout the world.

DØ has been actively seeking the top quark since 1992 when the detector was first commissioned at the Tevatron. Prior to the discovery paper, DØ published two search papers. The first set the world's highest lower limit of 131 GeV/c^2 for the top quark mass. After reoptimizing its analysis for a heavy top quark, DØ reported in the second paper nine events with an estimated background of 3.8 ± 0.9, too great a discrepancy to set a higher limit, but not sufficiently conclusive to declare discovery. This evidence for some top-like events led, near the end of 1994, to new analyses designed to identify a heavy top quark.

2.2 Top Quark Observation

If the top quark has a mass of about 200 GeV/c^2, theory predicts a production cross section of only 2–3 pb, about one hundred times less than that of one of the biggest backgrounds, W boson production.

The standard model predicts that almost 100% of the produced top quarks will decay to a W boson and a b quark. Top quark pair decays are therefore classified by the decay of the two W bosons ($W \to q\bar{q}$ or $W \to \ell\nu$). The search and observation of $t\bar{t}$ events is divided into three channels: the dilepton channel ($t\bar{t} \to \ell\bar{\nu}b\ \bar{\ell}\nu\bar{b}$), the lepton plus jets channel ($t\bar{t} \to \ell\nu b\ q\bar{q}\bar{b}$), and the all jets channel ($t\bar{t} \to q\bar{q}b\ q\bar{q}\bar{b}$).

The dilepton channel has the smallest background, primarily WW production and W plus jet events with fake leptons. Unfortunately, only 5% of $t\bar{t}$ events decay to e or μ. The lepton plus jets channel contains 30% of $t\bar{t}$ decays but has a much larger background, primarily due to the W plus jets production. Constraints on jet multiplicity, event topology and/or b-quark tagging, are required to extract a top quark signal. The third channel, the

Decay Mode	Number of Events	Background	Significance
Dilepton	3	0.65 ± 0.15	0.03 (1.9σ)
Lepton plus jets (topological)	8	1.9 ± 0.5	0.002 (2.9σ)
Lepton plus jets (b–tag)	6	1.2 ± 0.2	0.002 (2.9σ)
All	17	3.8 ± 0.6	2.0×10^{-6} (4.6σ)

Table 1: The number of events observed, background predicted, and the probability that the background fluctuated up to the observed data for each channel.

all jets channel, contains the largest fraction, 44% of all $t\bar{t}$ events, but the QCD multijet backgrounds are huge.

In its discovery paper, DØ published the observation of the top quark based on the analysis of the 1992-93 data combined with the first portion of the 1994-95 data. This analysis relied on the dilepton and lepton plus jets channels; the backgrounds in the all jets channel are so large that a signal had not yet been extracted. In the single lepton analyses, two independent strategies were used; in one, the topological differences between the top signal and the primary backgrounds were exploited (using the large solid angle coverage of the DØ detector). In the second, direct evidence for the presence of a b jet through its decay to a muon plus a residual jet was used.

Table 1 lists the number of events observed in the data and the predicted background for each $t\bar{t}$ decay channel. It also gives the probabilities for the predicted background to fluctuate up to account for the observed data. If the channels are combined, taking correlations into account, DØ determines the probability of the background fluctuating upwards to at least the number of observed data events to be

$$\mathcal{P} = 2.0 \times 10^{-6},$$

which is 4.6σ for a Gaussian distribution. This analysis established the existence of the top quark and determined the $t\bar{t}$ production cross section to be $\sigma_{t\bar{t}} = 6.3 \pm 2.2$ pb (for m_t= 200 GeV/c^2). The measured cross section and the distribution of events among the decay modes are consistent with predictions (see Section 3.4.2).

In addition to this analysis, which uses restrictive selection cuts to yield small background and large significance for a top signal, DØ used a looser selection to obtain 34 events but with larger background. For each of the channels, the cross section deduced from this loose selection agreed well with the tight selection, indicating that backgrounds are well understood.

Further verification that the observed signal is due to the top quark came from first evidence (in the discovery paper) that the single lepton channel events contained an additional W boson decaying into two quarks (jets). This second W is expected for top, but is not present for the background processes (see Section 2.4).

Subsequently a slight excess of events in the all-jets channel, consistent with that of the dilepton and lepton plus jets channels, has been observed.

2.3 Top Quark Mass

Having observed the top quark, a crucial issue for confronting the standard model is that of its mass. With six final state fermions as a result of the $t\bar{t}$ decay, there are eighteen momentum components to be determined. The problem can be constrained by requiring the top and anti-top masses to be equal, and the decay products of the W to reconstruct to give the W boson mass. If the W decay constituents and the b quark jets are unambiguously identified, at least fifteen of the momentum components must be measured to completely describe the event. With more, a constrained fit for the mass of the top can be attempted.

2.3.1 The Lepton plus Jets Channel

In the lepton plus jets channel, the analysis begins by looking for the decay $t\bar{t} \rightarrow \ell\nu b\ q\bar{q}\bar{b}$, which means every event should have at least four quark jets. (In practice, primary quark jets may escape detection, and additional jets arising from gluon radiation may increase the jet content of the event.) We use the three momenta of the four most energetic jets, the lepton, and the missing energy, a total of 17 components. Unless the b jets are identified, we must assign every jet in turn to every possible parton, which gives twelve possible combinations. The two-fold ambiguity for the longitudinal momentum of the neutrino means there are a total of 24 possible combinations for each event.

We apply the constraints that the top and anti-top masses be the same and that the two light quarks and the lepton and its neutrino match reconstruct to a W boson. With this prescription we can do a constrained fit to the $t\bar{t}$ system. We apply a cutoff in the fit quality (χ^2); events which do not have a jet assignment combination with a χ^2 below the cutoff are dropped from the m_t results. Finally, the central mass is obtained from best three χ^2 fits for each event. The result is termed the 'fitted mass'.

DØ extracts the top mass from the fitted mass distribution of its event sample using a likelihood fit. The distribution of fitted masses is matched to template distributions from a $t\bar{t}$ Monte Carlo, generated for a range of top masses. All detector effects and biases from the fitting procedures are accounted for by the simulation. The top quark mass obtained is:

$$m_t = 199^{+19}_{-21}(\text{stat})^{+14}_{-21}(\text{syst})\ \text{GeV/c}^2$$

Extensive Monte Carlo study of the procedure was done to elucidate the broadening of the resolution and the difference between the input 'true' top mass and the fitted mass. The effects of jet combinatorics are the dominant reasons for producing the difference between fitted and true masses; the studies showed that these effects were similar for both electron and muon channels, as well as for the topological selection and b-tag selection. These effects were carefully evaluated and included in the systematic error estimate.

Figure 2(a) shows the fitted mass distribution for the DØ lepton plus jets events, taken from the loose selection criteria. The histogram represents the fitted masses of the observed events, and the solid curve represents the background and the top Monte Carlo combined. Note the clear separation of background and signal events, permitting a good top mass determination. Figure 2(b) shows the resulting likelihood fit, with an arrow indicating the best fit value. In this analysis using the loose selection, the background and top signal components are dominant at quite different fitted mass values. If the tight selection cuts,

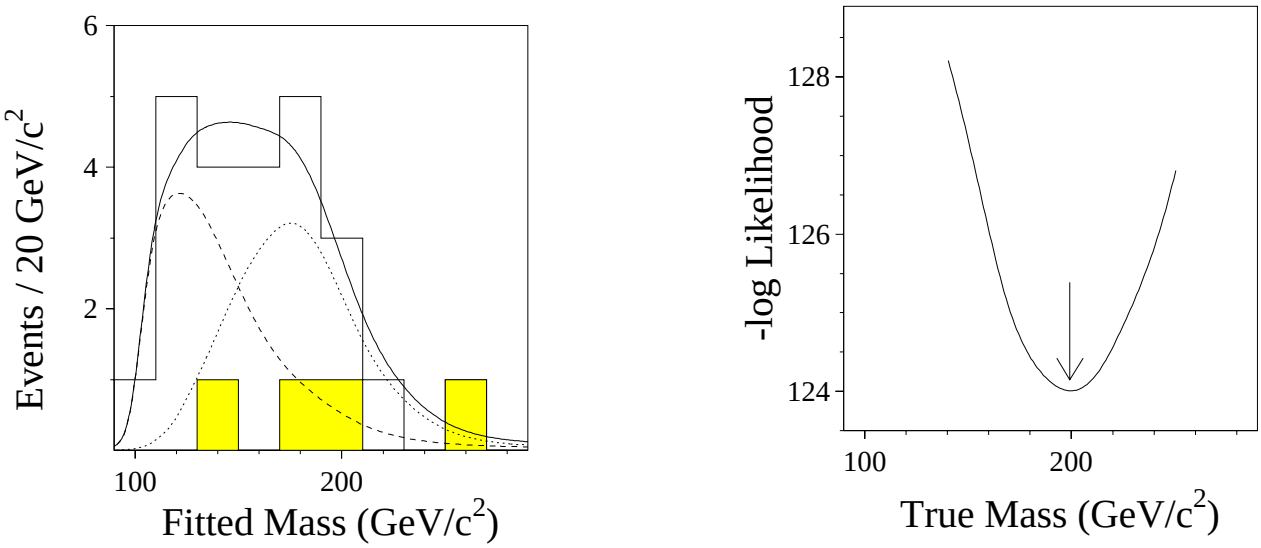

Figure 2: The fitted mass distribution (a) for events is shown as the line histogram, the dashed line is the background distribution and the dotted line is the best fit Monte Carlo fitted mass distribution. The solid line is the combination of the best fit Monte Carlo plus background. The shaded histogram represent events that were bottom quark tagged. The top mass is extracted from the fitted mass distribution using a likelihood method (b).

optimized for the observation analysis, are used, the background and signal distributions are more similar but the background is significantly smaller. The best top mass value for tight cuts is identical to that for the loose selection, but with slightly larger errors.

2.3.2 The Dilepton Channel

Finding the top mass in the dilepton channel is more difficult as we have less information; it is not possible to distinguish the two decay neutrinos, which are lumped together in the missing transverse energy. In order to provide additional probabilistic information, we use the knowledge of the initial state parton momentum distributions and the expected decay characteristics of the standard model top quark.

DØ uses a method, following those of Dalitz, Goldstein and Kondo, designed to utilize all the measured information and minimize the theoretical assumptions. We start by choosing a value for the top quark mass and assigning a weight based on known distributions of the transverse momentum of the lepton and structure functions for the valence quarks. The result is a likelihood curve as a function of m_t for each event, as shown in Figure 3(a). The most likely value of mass is retained as a characteristic parameter for each event.

Templates for the distributions of most likely masses are prepared from $t\bar{t}$ Monte Carlo and background samples. The best true mass is extracted using a likelihood method analogous to that used in the lepton plus jets analysis. Figure 3(b) shows the resulting best fit, where the arrows denote the peak of each individual event's likelihood curve, the dashed histogram is the background Monte Carlo distribution, and the solid is the fit for the best

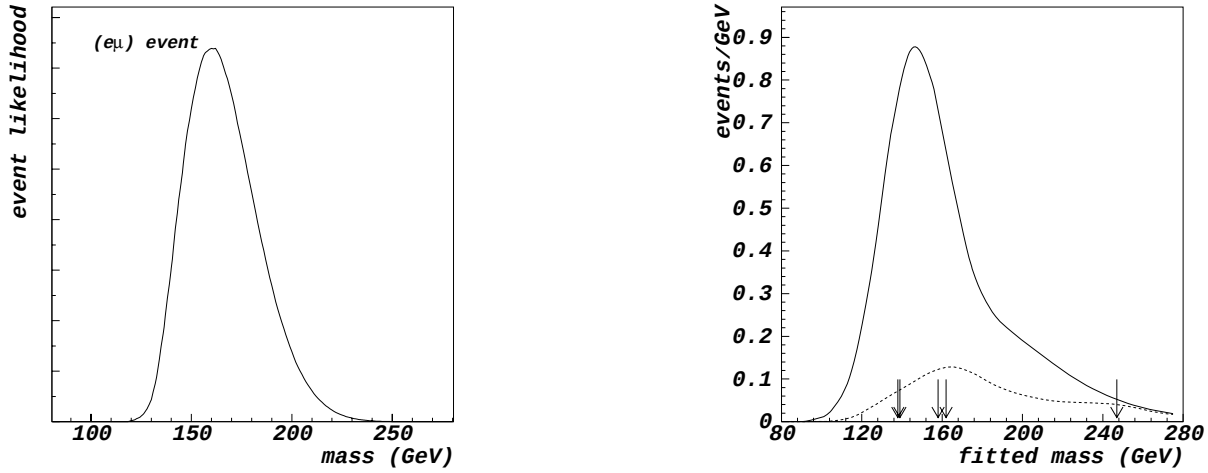

Figure 3: The dilepton mass fit method. The likelihood as a function of top mass for a particular event is shown in (a). The peak represents one of the arrows in (b), which is the fitted mass for all the dilepton events (arrows). The background fitted mass distribution is shown as the dashed line, and the best fit for background and Monte Carlo is shown as the solid line. The likelihood curve for the best mass has a broad minimum (not shown), leading to large errors on the mass.

value of the true mass. The likelihood is broad, and gives the result:

$$m_t \approx 145 \text{ GeV/c}^2 \text{ (preliminary)}$$

The statistical error deduced by examining the behavior of Monte Carlo samples of the same size is 25 GeV/c^2 while the systematic error is approximately 20 GeV/c^2, dominated by jet energy resolutions.

2.4 Top Quark Decays

The primary feature of top decays is expected to be the dominance of the bW final state. Both the observation and mass analysis use this to their advantage. In the lepton plus jets mass fit, for example, the light quark jets are constrained to the W boson mass. We would like to understand whether these expectations are well founded.

The distribution of events among the seven subchannels (with muons and electrons distinguished) is consistent at a confidence level of 53% with the expectations of the branching ratios for standard model top. If the W mass constraint is removed from the top mass fit, the mass moves by less than 7%. Thus good initial evidence for the appropriate aspects of top decay exists.

It should be possible to observe a W boson mass peak in the data when the W constraint is removed. The DØ data are shown in Fig. 4. The light histogram shows the data plotted vs. the reconstructed top mass (Fig. 4(a)) and dijet mass (Fig. 4(b)). The background distributions (solid histograms) do not represent the data well, while the sum of the background and Monte Carlo $t\bar{t}$ (gray histograms) agrees well with the data. Even if the known

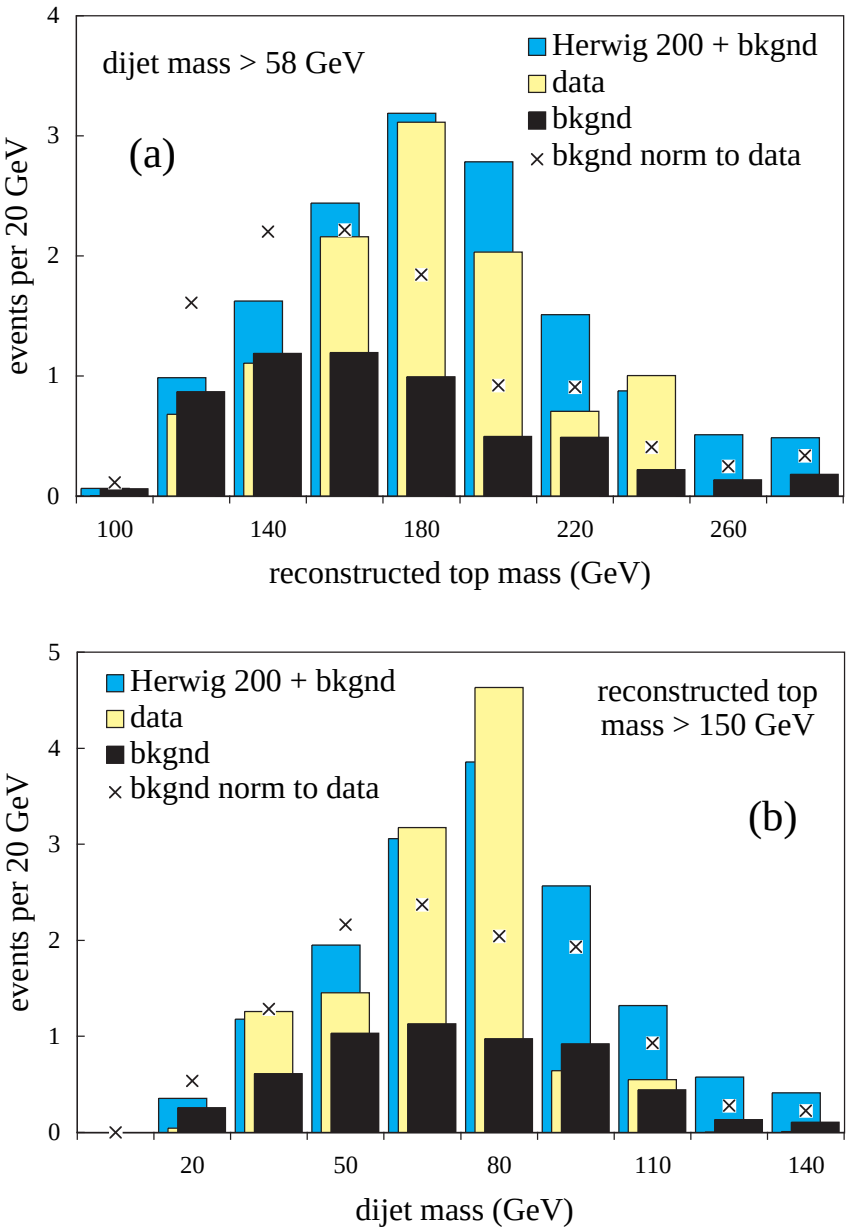

Figure 4: The reconstructed top mass and dijet mass spectra. A W boson mass peak can be seen in the the dijet mass distribution in data (light grey histogram). The black histogram represents the dijet mass distribution for background events, and the dark grey histogram is the distribution for the best combination for background and top Monte Carlo. The agreement between the best fit and the data is quite good, unlike the "×" histogram, which is the background normalized to the data.

normalization of the background is modified to give the total number of data events ("×"), the agreement is poor.

The enhancement of the dijet mass in the vicinity of the W boson mass should occur for the events for which the calculated top mass (either $t \to W(\ell\nu)b$ or $t \to W(\text{jet jet})b$) is near the measured top mass. Figure 5 shows a two dimensional histogram of calculated top mass (the average of the leptonic and hadronic decay top systems) and the dijet mass from the hadronically decaying top. The number of top events found in fits to these two-dimensional histograms without a constraint on the W to two jets agrees well with the standard analysis. The localization of events in the two dimensional region around the known W mass for the dijets and the top mass gives the most solid evidence to date for the presence of W bosons in top decay.

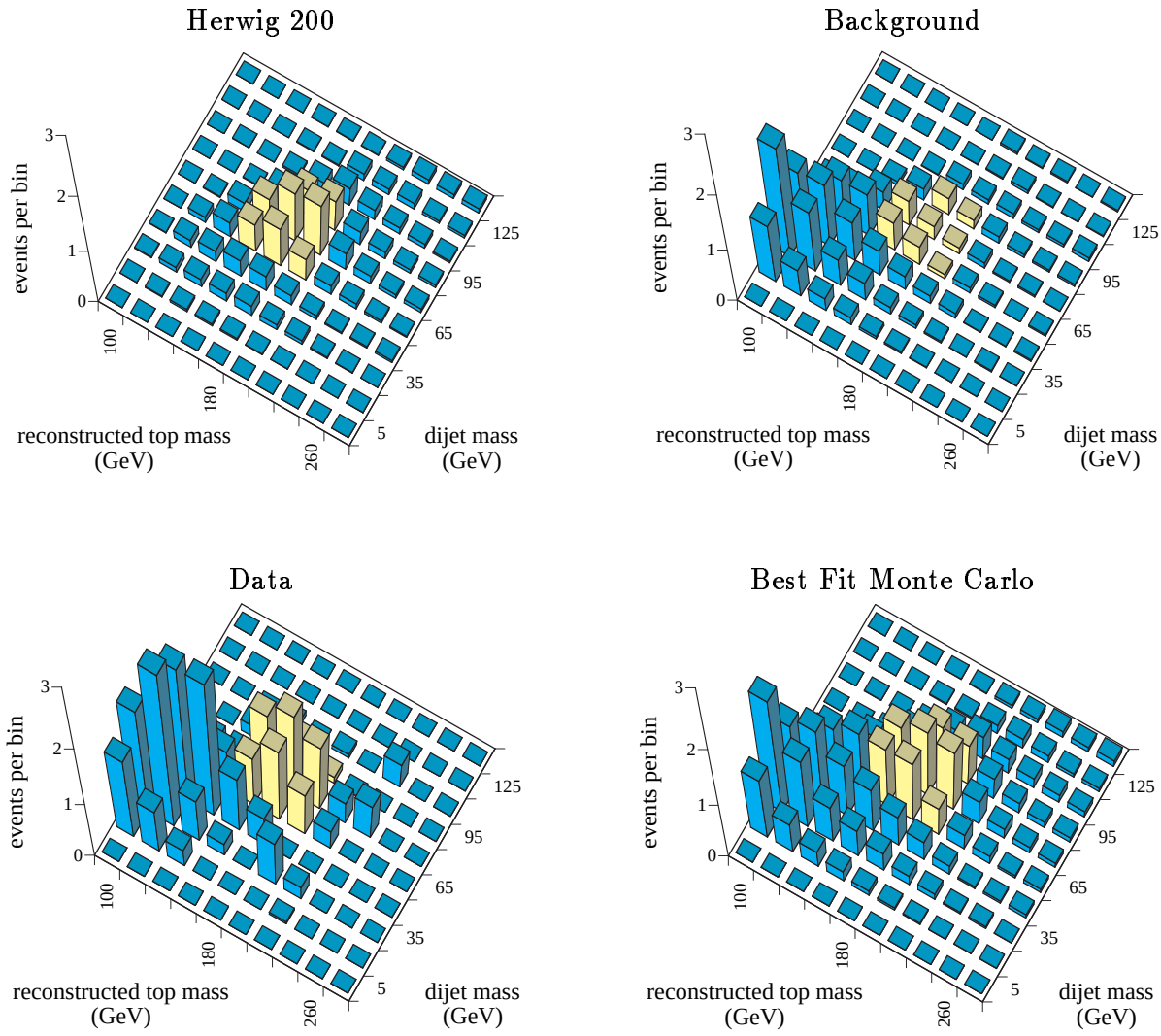

Figure 5: The correlations between the dijet mass and the reconstructed top mass in top events. For all histograms the same bins are highlighted to show the presence or absence of the top signal. The first plot is $t\bar{t}$ Monte Carlo which peaks in the highlighted area. In the next plot, the background distribution peaks away from the highlighted bins (the background is QCD data events and VECBOS W plus jet Monte Carlo). The data, shown in the third plot, shows that the event sample is a mix of background and signal. The final plot is the best combination of background and 200 GeV/c^2 $t\bar{t}$ Monte Carlo consistent with the data distribution.

3 Strong Interactions

The quantum chromodynamics (QCD) ($SU(3)_c$) description of strong interactions has its genesis in the deep inelastic scattering experiments of the late 1960's. Initial experiments attempted to elucidate and quantify the scaling violations of the parton distribution functions, using the electroweak bosons as probes, and extracted the strong coupling constant α_S.

In high energy interactions at a $p\overline{p}$ collider a typical measurement is described in perturbative QCD by the convolution of the parton distribution functions (pdf) with the hard scattering kernel. The program is well illustrated by the inclusive jet production cross section measurement shown in Figs. 6 and 7. The next-to-leading order (NLO) calculations agree within systematic errors at all pseudorapidities ($\eta = -\ln\tan(\theta/2)$ where θ is the polar angle with respect to the proton beam) with the DØ data. This agreement spans more than seven orders of magnitude of cross section for central jet production and five orders of magnitude for very forward jet production, a region unique to DØ. Theoretically, the prediction depends on both the evolution of the parton distributions and the hard scattering cross-section. The topologies of final states involving three and four jets have been studied and the agreement between the tree level predictions of perturbative QCD and the data is remarkably good.

DØ has investigated the strong interaction using jets and heavy quarks, the b- and t-quarks, whose large masses are hoped to ensure reliability of the perturbative predictions. The electroweak bosons, the photon, W and Z, can all be observed as final state particles and, being colorless, offer special opportunities.

QCD is successful in describing many experimental results, but the calculational techniques are inherently difficult and recourse to approximations is often necessary. DØ is testing the most recent approaches to this problem with a series of measurements involving multi-gluon interference effects.

3.1 Partons and Jets

The fundamental objects for QCD calculations are often quarks or gluons, observed in the real world as jets of hadrons. Calculations at the parton level, which ignore fragmentation, describe many experimental processes. The transformation from partons to jets has traditionally been described by phenomenological fragmentation models. Recently however there have been attempts to calculate the internal shapes of jets using perturbative QCD. The fine segmentation of the DØ calorimeter allows for a particularly detailed measurement of the structure of jets.

We have tested whether NLO partonic QCD predictions can accurately describe the shape of a jet by measuring the transverse energy flow within jets. Jets are divided into ten subcones around the jet axis with radii varying from 0.1 to 1.0 in $R = \sqrt{\Delta\eta^2 + \Delta\phi^2}$. The jet shape, $\rho(r)$, is defined as the fraction of transverse energy as a function of the subcone radius r. Figure 8 compares the experimentally measured jet shape to NLO predictions (JETRAD) for different renormalization scales, μ, in two different η regions. We see that NLO jet shape predictions are unable to accurately describe the experimentally measured jet shape for a particular value of renormalization scale over all kinematic regions and point to the need for

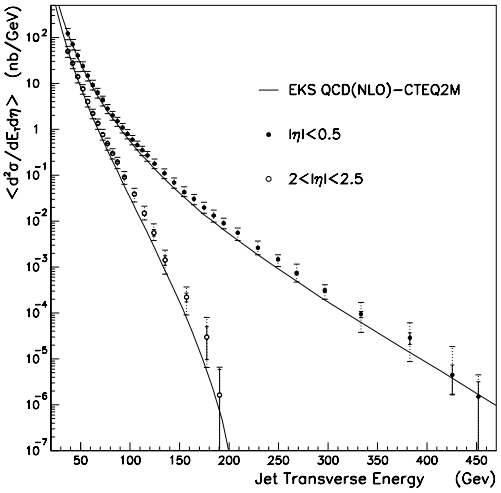

Figure 6: Preliminary inclusive jet cross section as measured at DØ for $|\eta| < 0.5$ and $2 < |\eta| < 2.5$. The data includes both statistical (solid) and systematic (dotted) error bars. The solid line corresponds to a smeared NLO QCD.

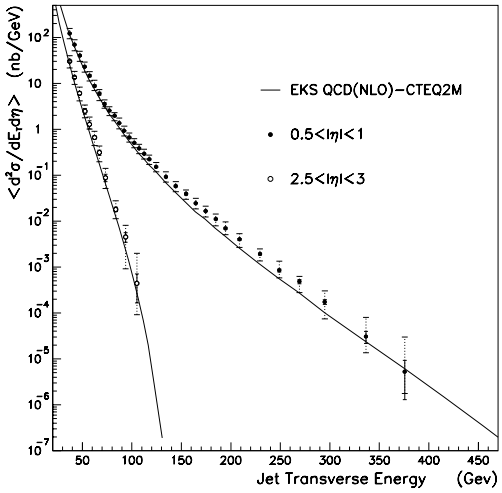

Figure 7: Preliminary inclusive jet cross section for $0.5 < |\eta| < 1.0$ and $2.5 < |\eta| < 3.0$. The error bars and NLO prediction are as in Fig. 6.

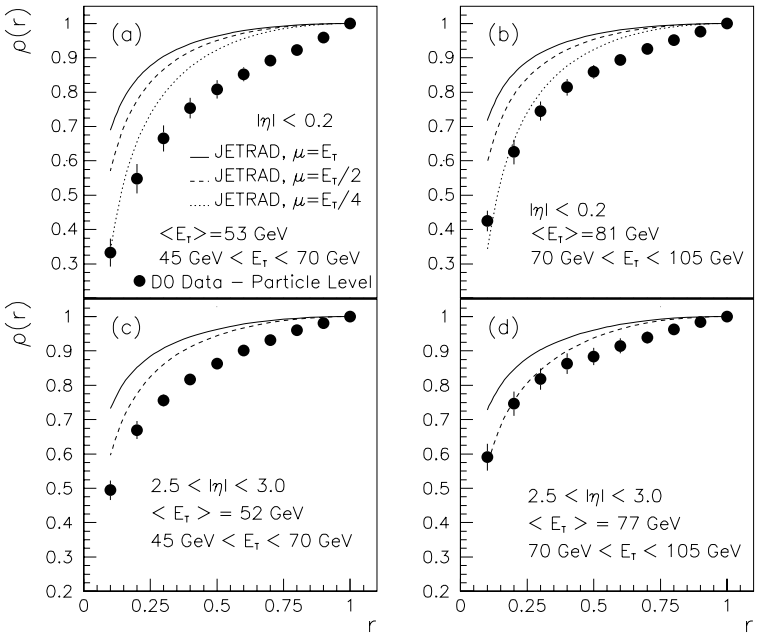

Figure 8: Transverse energy flow ($\rho(r)$) in a jet vs. r for central (a), (b) and forward (c),(d) jet samples. NLO QCD (solid and dashed lines) calculations do not reproduce the data.

higher order calculations.

Future analyses in this area will include comparisons to jet shapes measured in e^+e^- experiments. Preliminary results show jets at e^+e^- experiments to be narrower than jets produced at $p\overline{p}$ colliders. Monte Carlo studies suggest that quark jets are narrower than gluon jets. Since many more gluon jets are produced at $p\overline{p}$ colliders, this may explain the difference in shape between jets produced in $p\overline{p}$ collisions and e^+e^- collisions. Investigations of quark and gluon jet differences in the experimental data are underway, and it may be possible to discriminate between quark and gluon jets with reasonable efficiency. DØ has also presented preliminary measurements of jet substructure using the k_T algorithms for jet reconstruction which embodies the idea of a variable jet size definition.

3.2 Parton Distributions

Jet production cross-sections can be particularly sensitive to the parton distribution functions if the jet event systems span a sufficient range in η. The large coverage of the DØ calorimeter allows a unique measurement as shown in Fig. 9 where the η_1 vs. η_2 distribution of the two largest transverse energy (E_T) jets for a representative E_T bin is plotted. By measuring jets out to pseudorapidities of three, large ranges of the parton momentum fractions, ($0.005 < x < 0.75$), can be probed. No currently available set of parton distributions is able to model the shape of our preliminary results successfully. It is likely that, when incorporated into future global fits, these results will significantly modify our view of the gluon distribution. DØ has also presented measurements of the W boson production asymmetry which is sensitive to the ratio between the u and d quark distributions in the proton.

3.3 The Strong Coupling Constant

The running coupling constant α_S sets the strength of all strong interactions. The probability of producing jets in association with a W boson is dependent on its value. The DØ experiment has used the ratio, R, of the yield of W plus one jet to that of W plus zero jets to investigate this parameter.

Using our sample of $W \rightarrow e\nu$ candidates from the 1992–93 run, we compare the observed ratio to that predicted using specific pdf's and NLO QCD. Figure 10 shows the results of this study. The predictions using three different pdf's agree well with each other; however all of them give a ratio more than one standard deviation from our measured value. The dashed line represents the predicted ratio, as a function of α_S (for the CTEQ3M parton distributions) where α_S was varied only in the matrix element, leaving α_S in the pdf's fixed at the value of α_S produced by the global pdf fit. Similar results are obtained using the other pdf sets. Varying α_S in both the matrix element and the pdf's as illustrated by the symbols in Fig. 10 does not change the value of R substantially. Our current understanding of this insensitivity of the predicted ratio R to the value of α_S is that the softening of the gluon distribution compensates for the increase of α_S in the hard scattering matrix element. We will continue this study using the larger data set from the 1994–95 run and expanding the measurement to include the W plus two jets to W plus one jet ratio.

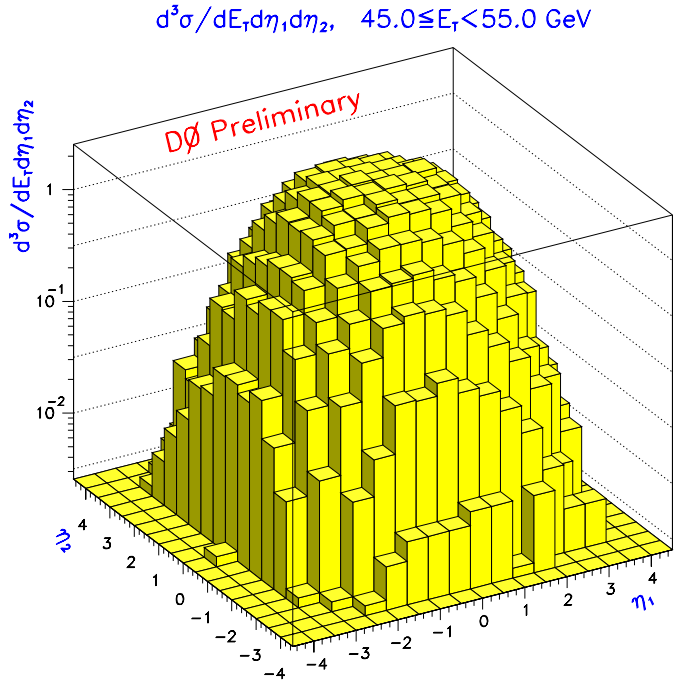

Figure 9: Triple differential jet cross section, $d\sigma/dE_T d\eta_1 d\eta_2$, measured for $45 < E_T < 55$ GeV, extending out to pseudorapidities of three.

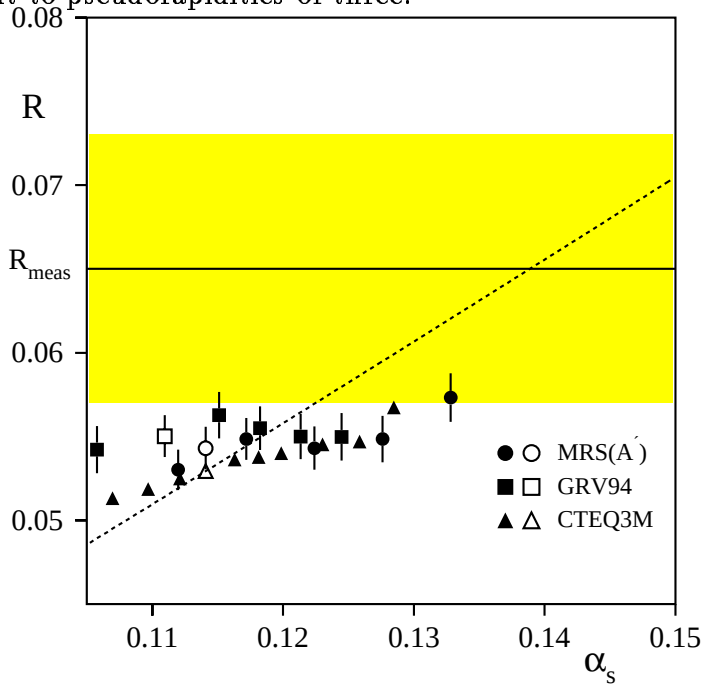

Figure 10: R vs α_S for CTEQ3M, MRS(A'), and GRV94 pdf's fitted with various values of ${\alpha_S}^{pdf}$. The open symbols correspond to the best fit for each pdf set. The dashed line is the prediction for CTEQ3M pdf when α_S is only varied in the matrix element.

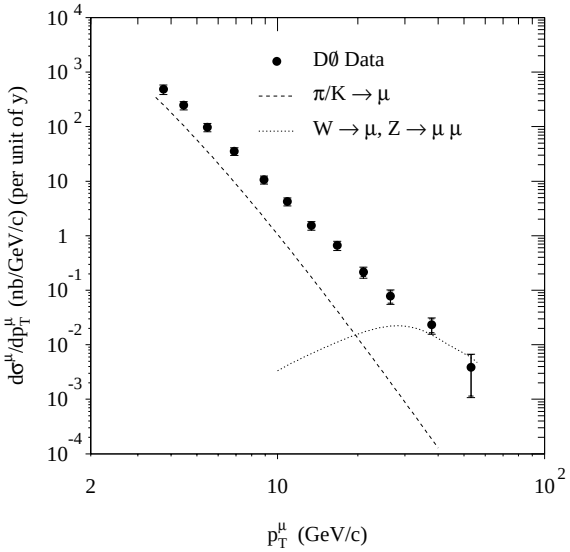

Figure 11: Inclusive muon spectrum for $\mid \eta^{\mu} \mid < 0.8$.

3.4 Heavy Quark Production

The study of b- and t-quark production at the Fermilab Tevatron provides an excellent testing ground for the details and procedures of perturbative QCD. The relatively large quark masses imply that theoretical calculations should be more reliable than for light-parton processes.

3.4.1 b-Quark Production

The hadroproduction of b-quarks has recently been the subject of intense studies, both theoretical and experimental. Next-to-leading order calculations have been available for some time. The lowest order $\overline{b}$ production processes (s-channel gluon diagrams or t-channel quark exchange) are rivaled at large p_T by $\mathcal{O}(\alpha_s^3)$ diagrams including the t-channel gluon exchanges with subsequent gluon splitting and flavor excitation diagrams.

DØ identifies events with b production through the semileptonic decay of the b-quark into a muon and a jet. The muon system provides measurement of muon momenta above 3 GeV/c over a pseudorapidity range $\mid \eta^{\mu} \mid < 3.3$. The thickness of the calorimeter plus iron toroids reduces the hadron punchthrough background to a negligible level and allows for good identification of muons inside jets.

The cross section for b-quark production, as a function of the minimum transverse momentum of the quark, $p_T^{\rm min}$, has been measured from inclusive muon, muon plus jet, dimuon and J/ψ data samples.

Figure 11 shows the inclusive muon differential cross section for $|\eta^{\mu}| < 0.8$. While there are significant backgrounds in the low p_T region due to in-flight decays of pions and kaons in the central detector volume and in the high p_T region due to muonic decays of the W and Z bosons, the cross section in the range $4 < p_T < 30$ GeV/c is dominated by heavy flavor (b and c-quark) production.

The b-quark content of the inclusive muon sample can be measured from the subsample of

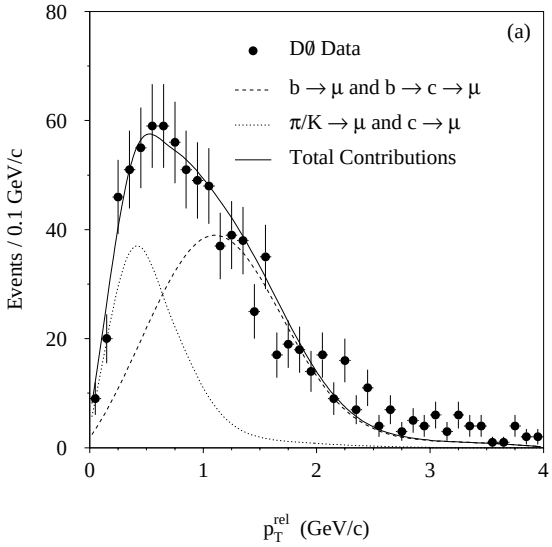

Figure 12: Transverse momentum of the muon with respect to the jet axis ($p_T^{\rm rel}$).

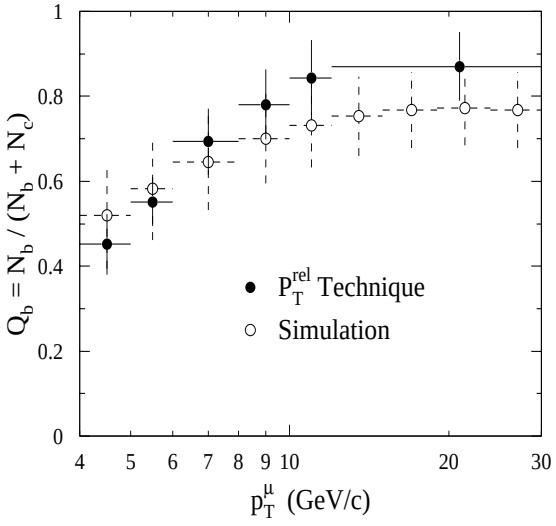

Figure 13: b-quark fraction in the inclusive muon sample.

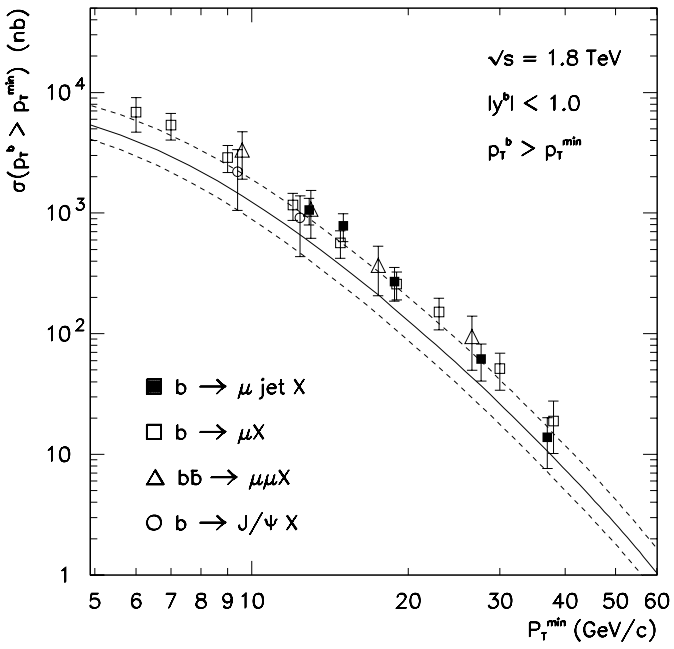

Figure 14: b-quark production cross sections for $\mid y^b \mid < 1$ from the inclusive muon, muon plus jet, dimuon and J/ψ data samples.

muons that are near or within a jet. Due to the high mass of the b-quark, the muon receives a higher transverse momentum "kick" in a muonic b-decay than the muon from the decay of the lighter c-quark. We quantify this transverse momentum "kick" with the variable $p_T^{\rm rel}$, the projection of the muon momentum perpendicular to the jet axis.

Figure 12 shows the $p_T^{\rm rel}$-distribution for the data and for b, c and in-flight decay Monte Carlo simulations. While the distributions from c and in-flight decays are similar, b-quark decays produce a distribution peaked at higher values of $p_T^{\rm rel}$. The fraction of b-production events in the inclusive muon spectrum for any interval of muon transverse momentum can hence be estimated by fitting the Monte Carlo $p_T^{\rm rel}$-spectra to the data, leaving the fraction of b-production as a free parameter in the fit. The result of these fits, shown in Fig. 13, agree very well with a Monte Carlo calculation of the b- and c-quark and decay-in-flight production cross sections.

In the last step of the analysis, a Monte Carlo method is used to convert the background subtracted muon spectrum into the b-quark production cross section in the b-quark rapidity range $\mid y^b \mid < 1$.

The b-quark production cross section was also measured from a dimuon sample. The data are selected to be in the dimuon invariant mass range of 6 to 35 GeV/c^2 to reduce background from J/ψ-mesons and Z-bosons. Backgrounds from Υ and Drell-Yan decays are further reduced by requiring a nearby jet. The b-fraction in this data sample is calculated by simultaneous maximum likelihood fits to the $p_T^{\rm rel}$ distributions of the higher p_T (leading) and lower p_T (trailing) muons in each event. We find that b-production contributes to over 75% of the dimuon sample above p_T= 5 GeV/c for the leading muon.

The b-quark production cross sections for $\mid y^b \mid < 1$ from the inclusive muon, muon plus

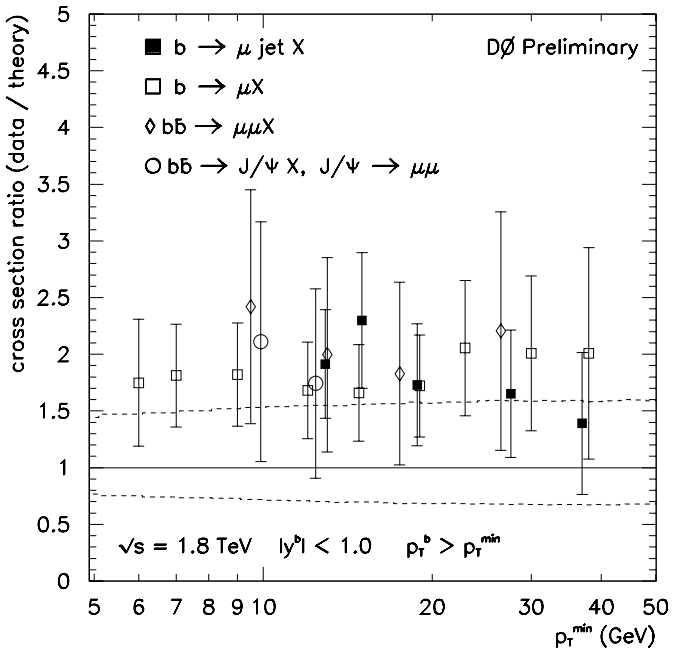

Figure 15: Ratio Data / Monte Carlo for DØ b-quark production cross section measurements. The data points from Fig. 14 are divided by the central NLO QCD cross section calculation.

jet, dimuon and J/ψ (see Section 3.5.1) data samples are shown in Fig. 14 and are compared to NLO QCD predictions. The upper limit on the systematic error in Fig. 14 is computed assuming the renormalization and factorization scale is half the value used for the central value. The data favor smaller values of the renormalization and factorization scale μ.

The ratio of the measured cross sections to the central value of the NLO QCD predictions is shown in Fig. 15. The measured cross sections are approximately a factor of two larger than their predicted values for the entire range of $p_T^{\min}$ studied. DØ is in the process of collecting data at $\sqrt{s} = 630$ GeV to investigate the energy dependence of the b-quark cross sections.

3.4.2 t-Quark Production

Having observed the top quark, and measured its mass, we can determine the cross section for $t\bar{t}$ production. Figure 16 shows the theoretical cross section, DØ's measured cross section as a function of m_t, and the DØ mass point where the cross section is:

$$\sigma_{t\bar{t}} = 6.3 \pm 2.2 \text{ pb}$$

The measured cross section is less than one standard deviation from the theory calculation. The cross section for each of the individual channels, along with the combined result, is shown in Fig. 17. The cross section from the individual channels are consistent with the overall result, which indicates we see top in all channels.

The high top quark mass, at about the electroweak symmetry breaking scale, has inspired speculation that there may be clues to physics beyond the SM in the production spectra for

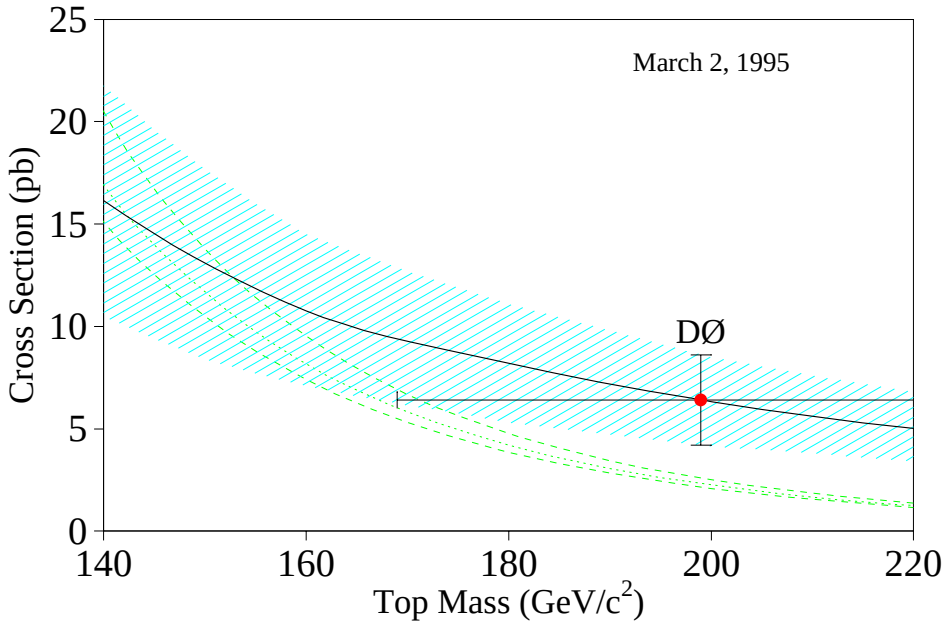

Figure 16: The cross section for $t\bar{t}$ production as a function of the top mass. The narrow shaded band is the theory cross section (Laenen, Smith, and van Neerven) with errors. The broad band is the DØ measurement. The point represents our mass and cross section measurements with errors.

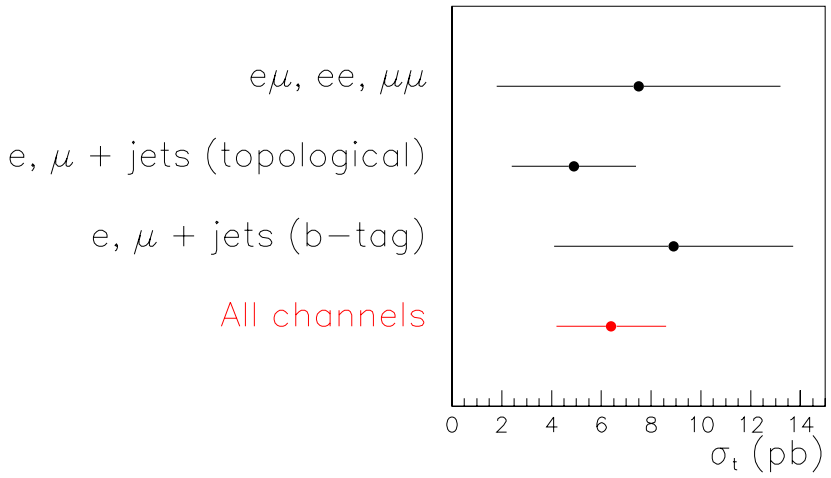

Figure 17: The cross sections from individual channels are consistent with the combined cross section result, indicating that we see top in each channel.

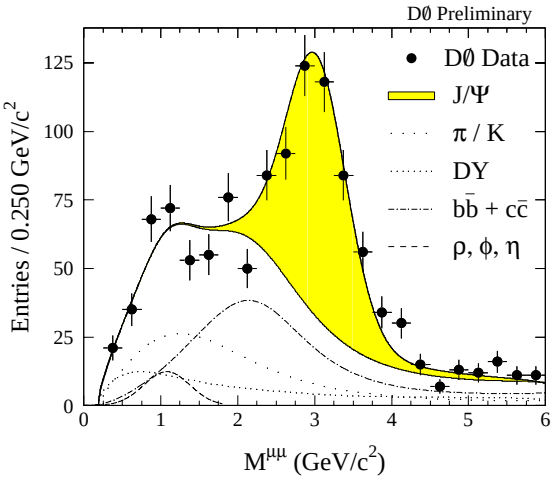

Figure 18: The mass spectrum for opposite sign muon pairs in the central region. The solid curve is the fitted sum of the J/ψ signal and background contributions, which are also shown separately.

top. Possible $t\bar{t}$ resonances associated with technicolor or other new dynamical symmetries have been suggested. DØ has studied various kinematic distributions of the $t\bar{t}$ system and compared them with expectations. The distributions of total mass of the $t\bar{t}$ system, $m_{t\bar{t}}$, and the p_T of the $t\bar{t}$ system reveal no significant new physics at play.

3.5 Production of Onia

3.5.1 Charmonium Production

A $c\bar{c}$ state is the lightest bound system of quarks for which perturbative QCD is expected to apply. The J/ψ is of particular significance because of its clean signature through the dilepton decay modes. In high energy $p\overline{p}$ collisions the dominant contributions to the J/ψ production are expected to come from the lowest order Feynman diagrams with gluon-gluon fusion, either directly into charmonium and a recoiling gluon, or through a $\overline{b}$ pair followed by a decay $b \rightarrow J/\psi X$. It has recently been argued that in addition to the gluon-gluon fusion, the process of gluon fragmentation (the splitting of a virtual gluon into a charmonium state and other partons) is an important source of J/ψ.

There are several processes contributing to the dimuon mass spectrum shown in Fig. 18. They include J/ψ direct production and charmonium state decays. Contributions from the different processes were measured by a simultaneous maximum likelihood fit of the invariant mass of the dimuon pair; of an isolation parameter quantifying the presence of hadronic energy deposition in the calorimeter near the dimuon; and if a jet is reconstructed, of a $p_T^{\rm rel}$-parameterization of the dimuon axis with respect to the jet.

The dimuon data and the results of the fit are shown in Fig. 18 together with the fitted contributions from J/ψ production and backgrounds. The differential cross section for J/ψ production is shown in Fig. 19, compared to calculations for the various production mechanisms. Our measured J/ψ cross section can be adequately described by theoretical predictions that include direct charmonium production, b decay, and gluon and c-quark fragmentation.

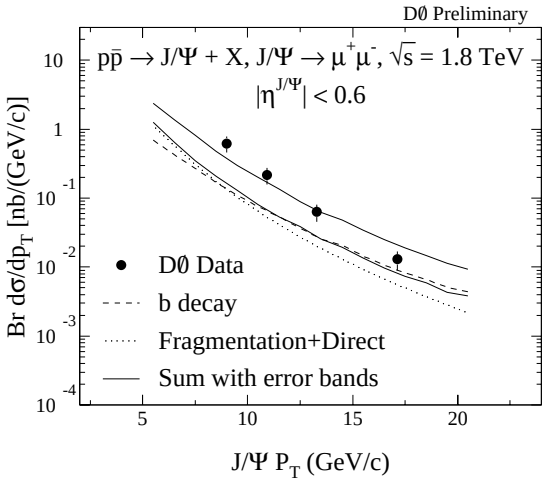

Figure 19: The product $BR \cdot d\sigma/dp_T$ vs p_T for $J/\psi \rightarrow \mu^+\mu^-$. The dotted line corresponds to J/ψ production through B meson decays. The dashed line corresponds to the prompt J/ψ production. The sum, with theoretical uncertainties, is indicated by the solid lines.

In addition, the coverage of the DØ detector in the forward region allows us to observe for the first time J/ψ production in the forward rapidity range. The invariant mass of the dimuon sample in the region $2.6 < |\ \eta^{J/\psi}\ | < 3.4$ is shown in Fig. 20. Figure 21 shows the J/ψ production cross section as a function of pseudorapidity for $p_T^{J/\psi} > 8$ GeV/c.

The contribution of various J/ψ production mechanisms to the J/ψ cross section has been investigated. Due to the lifetime of the B-meson ($\sim$ 1 ps) the J/ψs from b-decays are produced away from the event vertex, while those from direct charmonium production and fragmentation processes are produced at the event vertex. In the central region the fraction of b-produced J/ψs, was measured to be $(35 \pm 9 \pm 10)\%$ from the the muon impact parameter distribution with respect to the event vertex. The b-quark production cross section extracted from this data sample is shown in Fig. 14.

Measuring events with photons associated with J/ψs can be used to estimate J/ψ production from radiative χ_c decays. The χ_c signal is shown in Fig. 22. Photons from χ_c decays have energies of order 1 GeV and their reconstruction is a demanding technical test of the DØ electromagnetic calorimeter performance. We estimate that $(30 \pm 7 \pm 7)\%$ of J/ψs with $p_T > 8$ GeV/c and $|\ \eta\ | < 0.6$ are due to χ_c production.

3.5.2 Bottomonium Production

It is interesting to investigate whether bottomonium (Υ) production, analogously to charmonium production, has production mechanisms in addition to gluon-gluon fusion into χ_b states which radiatively decay into Υ and parton-parton scattering into Υ or χ_b states.

Main backgrounds to the Υ signal are QCD ($\overline{b}$, $c\bar{c}$ and π/K) production, Drell-Yan production, and cosmic ray muons. The signal and background contributions were resolved using a maximum likelihood fit to the data and the differential cross section $BR \cdot d\sigma/dp_T$ is extracted using the results of the fit. The dimuon p_T distribution for all events is summed

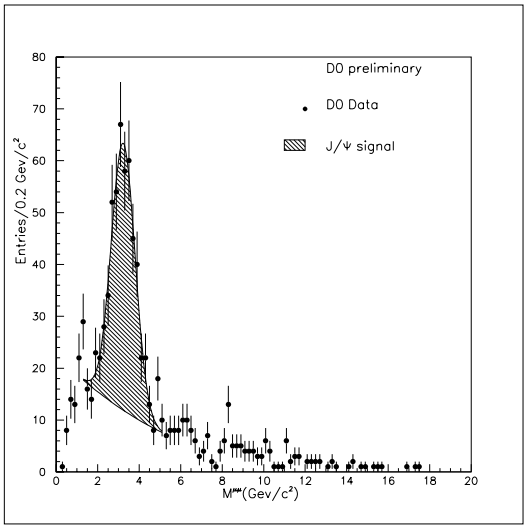

Figure 20: Dimuon invariant mass distribution in the forward region.

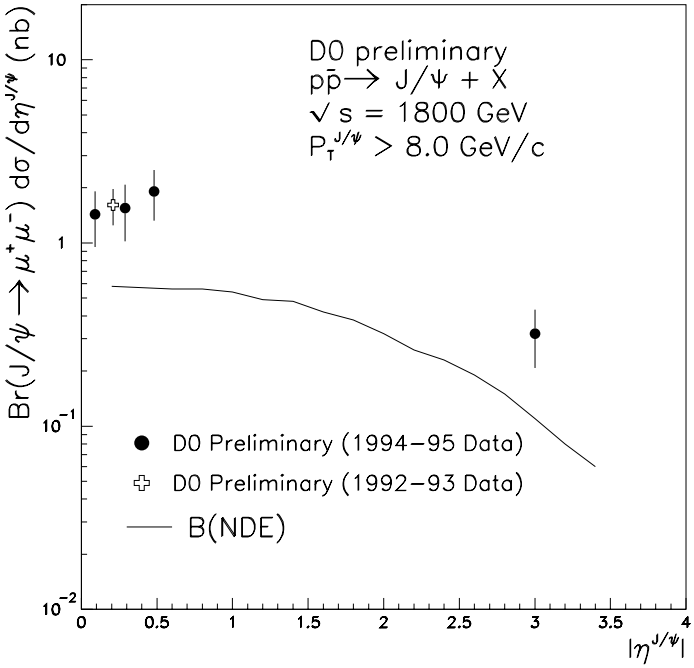

Figure 21: J/ψ production cross section as a function of the pseudorapidity of the J/ψ meson, for $p_T^{J/\Psi} > 8\,\mathrm{GeV/c}$.

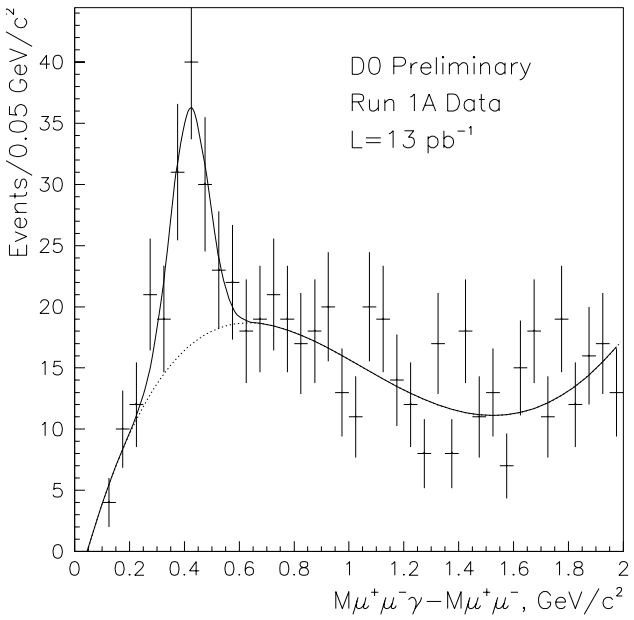

Figure 22: Distribution in $\Delta M = M(\mu\mu\gamma) - M(\mu^+\mu^-)$ for dimuon pairs in the J/ψ region.

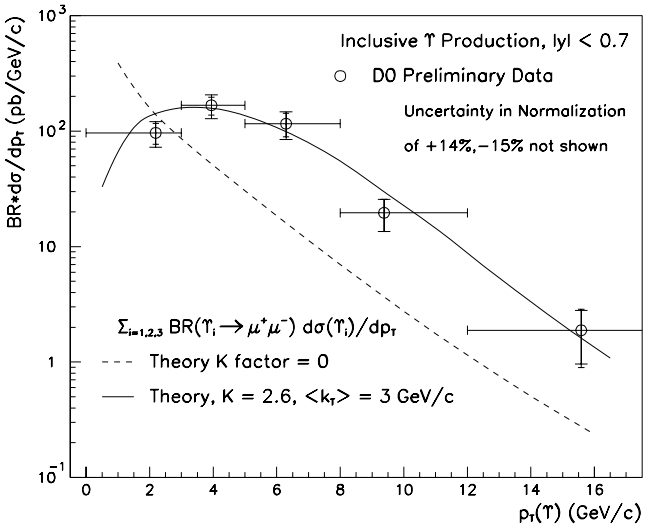

Figure 23: $BR \cdot d\sigma/dp_T$ for $|y^\Upsilon| < 0.7$. There is an additional $^{+14}_{-15}\%$ systematic error for p_T independent sources which is not included in the figure.

with each event weighted by the probability that it is an Υ; the results are shown in Fig. 23. Note that the cross section is a sum over all Υ S-states. Integrating the differential cross section gives a total cross section $BR \cdot d\sigma/dy|_{y=0} = 1.88 \pm 0.99 \pm 0.92\,\mathrm{pb}$.

The NLO predictions shown in Fig. 23 are roughly a factor of 5 lower than the data for $p_T^\Upsilon > 5$ GeV/c and diverge as $p_T^\Upsilon \to 0$. Good agreement between data and theory can be achieved by assuming an average initial state parton k_T of 3 GeV/c and a rather large K

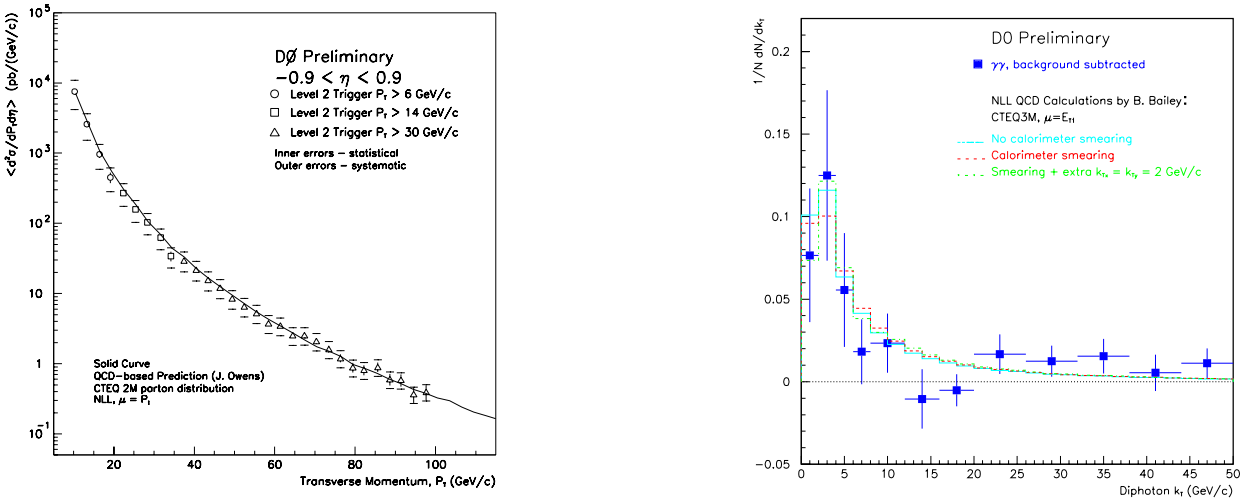

Figure 24: (a) Inclusive photon cross section for $|\eta| < 0.9$ with statistical (inner) and systematic (outer) error bars. The smeared NLO QCD prediction (solid line) agrees well with the data. (b) Preliminary diphoton k_T distribution with background subtracted. The lines show the smeared and unsmeared NLO predictions.

factor of 2.6.

3.6 Photon Production

Direct photons provide an interesting probe of QCD because, unlike jets, they are not subject to final state interactions, they can be relatively unambiguously identified, and their energy is measured accurately. Unfortunately, photons also suffer from a large background from jets which fragment into electromagnetically interacting particles.

A preliminary cross section for the inclusive production of central, isolated direct photons has been measured by DØ and is shown in Fig. 24(a). The background contribution has been estimated using the longitudinal and transverse shower shape, and by measurement of photon conversions in the drift chambers. After background subtraction, the photon cross section is in good agreement with a NLO QCD calculation.

DØ has also measured a preliminary cross section for production of diphotons, which is in good agreement with the NLO QCD prediction. Figure 24(b) shows the diphoton k_T spectrum, the intrinsic transverse momentum of the incoming partons. The agreement of data and prediction suggests that no extra k_T beyond that included in NLO is necessary.

3.7 W/Z Production

The transverse momentum of intermediate vector bosons produced in $p\overline{p}$ collisions is provided by initial state gluon radiation. In the low transverse momentum region ($p_T < 20$ GeV/c) multiple soft gluon emission is expected to dominate the initial state radiation and the production cross section is calculated using a soft gluon resummation technique. In the high

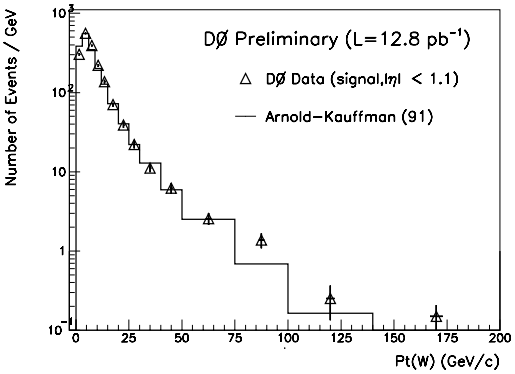

Figure 25: Multijet background subtracted W p_T distribution for $|\eta| < 1.1$ (triangles) with smeared theoretical prediction (histogram) superimposed.

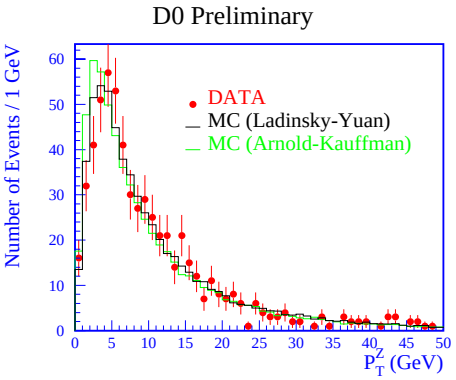

Figure 26: Multijet background subtracted Z p_T distribution (points). The smeared predictions of Arnold and Kaufmann (dashed line) using HMRSB pdf's and Ladinsky and Yuan (solid line) using CTEQ2M are superimposed.

p_T regime ($p_T > 20$ GeV/c) the cross section is expected to be well described by perturbative QCD calculations. Thus a measurement of the transverse momentum distributions may be used to constrain the resummation calculations in the low p_T range and to test the perturbative QCD predictions at high p_T. Deviations from the prediction at large p_T could be an indication of new physics.

In the analysis of both W and Z samples, the multijet background was subtracted. The results are shown in Figs. 25 and 26 with theoretical predictions smeared to reflect detector response superimposed. Significant deviations at lower p_T, the region where the soft gluon resummation techniques are used, are seen.

3.8 Gluon Interference

Until recently most of the quantitative comparisons between data and QCD calculations have been limited to rather low orders in the calculation and to relatively simple experimental measurements. However at the level of multi-gluon emission there are numerous beautiful interference effects expected which depend in detail on the real structure of the theory. Below we describe three measurements which explore this behavior.

3.8.1 Color Coherence

Color coherence phenomena have been observed in experiments studying the angular flow of hadrons in three jet events from e^+e^- annihilations. Color coherence effects arise from the constructive and destructive interference of soft gluon radiation emitted along the color connected partons. In $p\overline{p}$ collisions we study initial-final state color interference effects by

measuring spatial correlations between soft and hard jets in multijet events.

We selected three jet events where the leading (highest E_T) jet has very high E_T and the second leading jet is in the opposite ϕ hemisphere from the first. The angular distribution of the softer third jet around the second highest E_T jet in (η, ϕ) space is studied using the angular variable β, measured in the plane defined by the second jet and the beam. The beam directions correspond to $\beta = 0$ and π, while $\beta = \frac{\pi}{2}$ and $\frac{3\pi}{2}$ correspond to the directions perpendicular to the beam. The expectation from interference effects is that the rate of soft jet emission in the regions $\beta = 0$ and π will be enhanced relative to the $\beta = \frac{\pi}{2}$ and $\frac{3\pi}{2}$ regions.

The data distributions are compared to three shower Monte Carlo event generators, two which incorporate color coherence effects by means of an angular ordering approximation (HERWIG and PYTHIA), and one that implements an independent shower development model (ISAJET). A NLO parton level prediction (JETRAD) is also compared to the data. The ratios of the data β distributions to the Monte Carlo predictions where the second jet was required to have $|\eta| < 1.5$ are shown in Fig. 27. The shower Monte Carlos that incorporate color coherence effects model the data rather well while the absence of color interference in ISAJET results in a disagreement with the data. The NLO prediction is also in qualitative agreement with the data which shows that these effects are perturbative in origin and present in the $2 \rightarrow 3$ matrix element. A complementary analysis is under way to study color coherence effects in much softer gluon radiation by measuring the energy flow patterns around the W and jet directions in W plus jet events.

3.8.2 Dijet Decorrelation

A new topic in perturbative QCD is the search for the BFKL pomeron. This object is the result of higher order effects interfering strongly over a spatially extended region of the proton to produce enhanced gluonic radiation. The DØ detector is well suited to study this phenomenon with its forward calorimetric coverage as this effect is larger when a high rapidity interval for gluon radiation is available. At the single center of mass energy available at the Tevatron, only indirect effects of this phenomenon can be probed.

In this study, we focus on the two jets with the largest rapidity separation in multijet events. It is precisely in this configuration where the gluonic radiation should be enhanced. We do not try to observe the radiation directly, but instead attempt to see indirect effects in the correlation in azimuth (ϕ) as these jets become more widely separated in η. We have parameterized the correlation in terms of the expectation value of $\cos(\pi - \Delta\phi)$. Completely correlated jets will have a value of $< \cos(\pi - \Delta\phi) > = 1$. As intervening gluon radiation weakens the correlation, the expectation value should approach zero. The results of this study are presented in Fig. 28 where we do indeed see an increase in decorrelation. We compare our results to three QCD predictions: a NLO parton event generator, a parton shower Monte Carlo, and a prediction incorporating the effects of the BFKL pomeron. From the figure we see that NLO QCD (JETRAD) does not produce enough decorrelation, the BFKL predictions produce too much, while the parton shower Monte Carlo (HERWIG) reproduces the data very well.

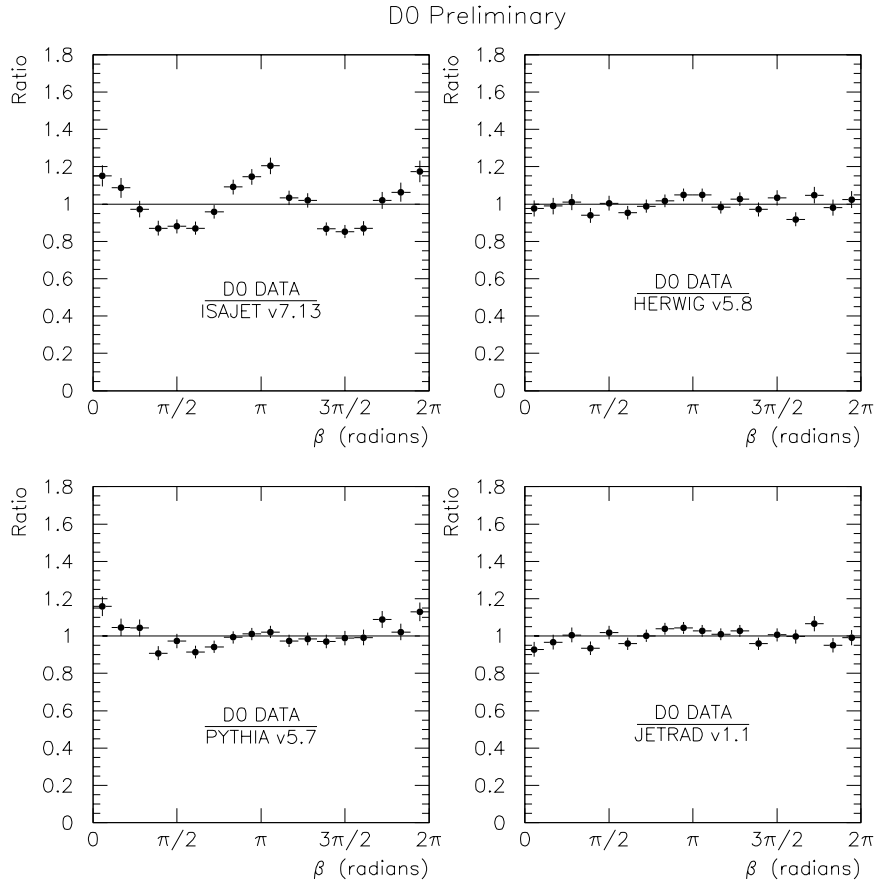

Figure 27: Ratio of the β distributions between data and Monte Carlo predictions for jets with $|\eta| < 1.5$.

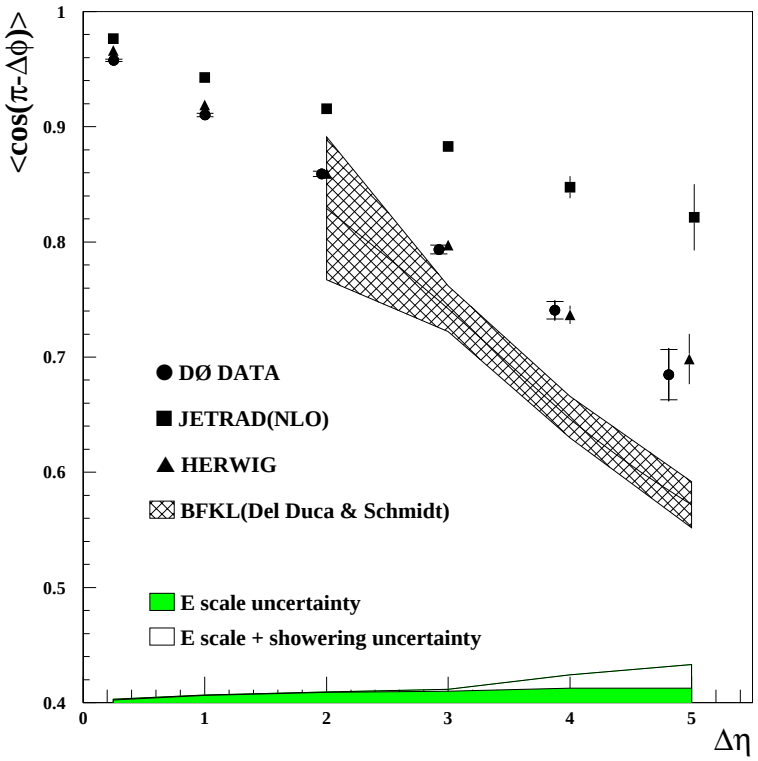

Figure 28: Dijet decorrelation parameterized as $< \cos(\pi - \Delta\phi) >$ vs. $\Delta\eta$. The parton shower Monte Carlo HERWIG does the best job reproducing the data.

3.8.3 Color Singlet Exchange

In this analysis we search for strongly interacting color singlet exchange by tagging events with a low multiplicity of particles between jets. Few particles are expected between the leading jets in color singlet events, whereas the presence of a color string connecting the scattered partons in color octet events (gluon exchange) gives rise to a smooth distribution of particles between the leading jets. In QCD the absence of particles as a result of strong color singlet exchange is a manifestation of the destructive interference between the emissions of gluons from two colored objects, the gluon components of the pomeron.

Two different data sets were used to study this effect: one selected events with the two jets on opposite sides of the calorimeter ($\eta_1 \cdot \eta_2 < 0$) while the other selected events with jets on the same side ($\eta_1 \cdot \eta_2 > 0$). The same side sample is expected to be dominated by color octet exchange and is used as a control. Figure 29 shows the number of electromagnetic calorimeter towers above threshold (n_{cal}) versus the number of central drift chamber tracks (n_{trk}) for the (a) opposite side and (b) same side samples. The two distributions are similar in shape except at very low multiplicities, where the opposite side sample has a striking excess of events, consistent with a color singlet exchange process. We measure this fractional excess of color singlet above color octet exchange to be 1.07 ± 0.10 (stat) $^{+0.25}_{-0.13}$ (syst)%. This value, while inconsistent with electroweak exchange alone, is consistent with the colorless exchange being the pomeron.

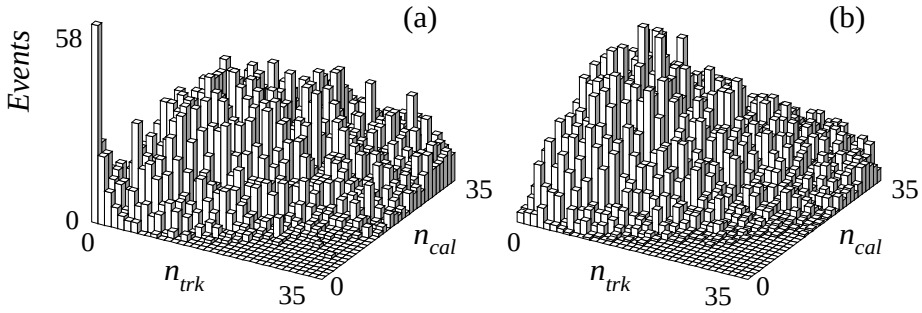

Figure 29: The calorimeter tower multiplicity (n_{cal}) vs. the charged track multiplicity (n_{trk}) in the pseudorapidity region $|\eta| < 1.3$ for the (a) opposite-side and (b) same-side samples described in the text.

4 Electroweak Physics

Electroweak theory, or the standard model of electroweak interactions, was the second successful theory unifying two different types of interactions after the famous Maxwell equations. It was developed in the 1960's by Glashow, Salam, and Weinberg and, since its first experimental confirmation through observation of the neutral currents, has become the leading theory describing both electromagnetic and weak forces.

Since 1983, when the intermediate vector bosons W and Z, the gauge field quanta of the SM, were discovered at CERN, numerous experiments have probed this theory and measured its few free parameters with increasing accuracy. Up to now, despite many theoretical attempts to extend the theory of the electroweak forces to incorporate new physics, no convincing deviation from the SM has been observed. However, extensive tests of this theory are very important, since the measurements have finally reached the level of accuracy allowing measurements of radiative corrections to the SM, as well as ruling out some alternative theories.

The SM is based on a fundamental $SU(2)_L \times U(1)_Y$ symmetry. There are four independent gauge fields which correspond to this symmetry: a non-Abelian $SU(2)$ field W^i, $i = 1, 2, 3$, and an Abelian $U(1)$ field B. The fermions are described in the theory as independent left-handed and right-handed fields. The left-handed fields are transformed as $SU(2)$ isospin doublets, whereas the right-handed fields are isospin singlets. There are no right-handed neutrinos in the SM.

The masses of the gauge bosons appear due to the local symmetry breaking via the Higgs mechanism which mixes W^i and B fields into the massless photon field A and three massive fields $W^{\pm}$ and Z.

The gauge sector of the SM is unambiguously fixed by a set of three independent parameters. Conventionally, the following parameters are used: the fine structure constant α, the Fermi coupling constant G_F, and the mass of the Z boson, all currently measured to a very high precision.

Since the W and Z bosons are heavy it is essential to have a high energy machine to copiously produce and thoroughly study these bosons. The Tevatron accelerator at Fermilab, operating at $\sqrt{s} = 1.8$ TeV, is therefore well-suited for studies of electroweak physics.

4.1 W and Z production cross sections

Measurement of the production cross sections times the leptonic branching ratios ($\sigma \cdot BR$) for W and Z bosons allows a test of the QCD predictions for gauge boson production. Using the width of the Z boson previously measured at LEP with 0.3% precision, these cross sections can be translated into the width of the W boson. Comparison of the measured W width with the SM prediction places a strong constraint on the existence of new particles produced in W-decays.

The production cross sections times leptonic branching ratios of the W and Z bosons were recently measured by DØ using the 1992–1993 data set. Transverse mass spectra of the W and invariant mass spectra of the Z candidates, for the electron and muon channels, are shown in Fig. 30. The estimated backgrounds to the W/Z production, dominated by QCD multijet production with jets faking leptons are represented by the hatched areas in

these plots. For the muon channel there are additional backgrounds from cosmic rays as well as the "leakage" of the $Z \to \mu\mu$ signal into the W sample due to the unreconstructed muons which fake missing transverse energy. The overall background is $\sim 5\%$ of the signal for electron channels, 10% for $Z \to \mu\mu$ and 20% for $W \to \mu\nu$ processes.

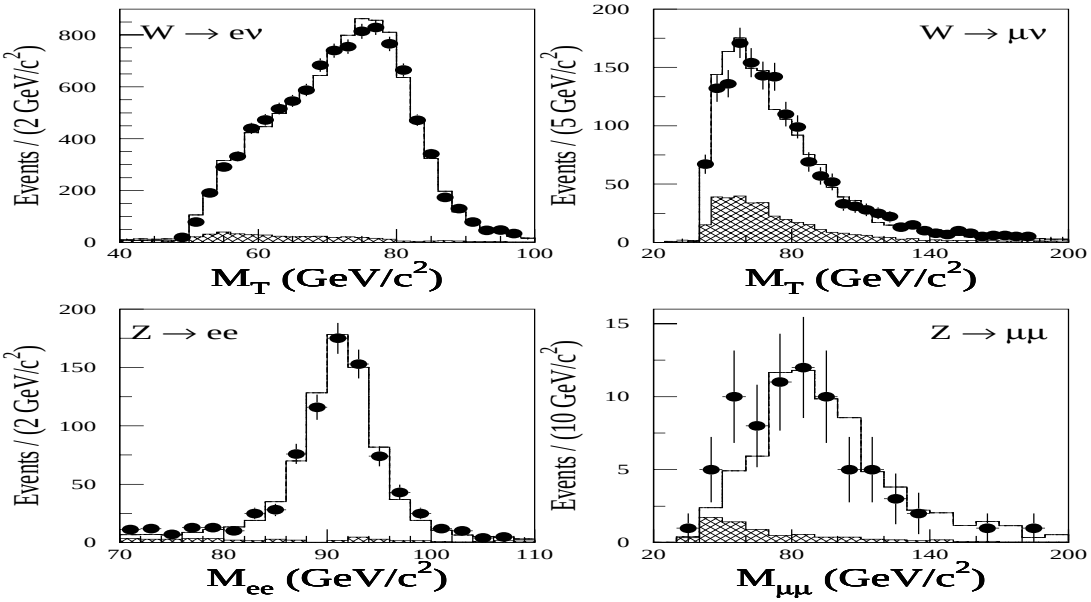

Figure 30: Transverse mass and invariant mass distributions for the indicated channels. The points are the data. The shaded areas represent the estimated backgrounds, and the solid lines correspond to the sums of the expected signals (from Monte Carlo) and the estimated backgrounds.

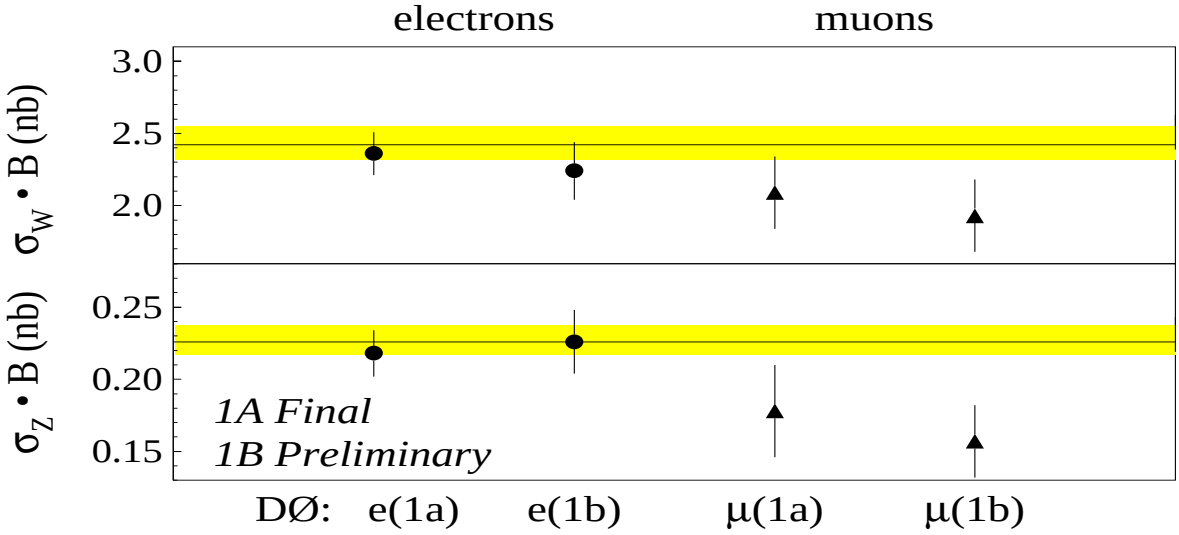

Figure 31: $\sigma \cdot BR$ for inclusive W and Z boson production. The solid line and shaded band are the theoretical prediction described in the text.

The cross section results are represented in graphical form in Fig. 31, together with preliminary measurements from the 1994–95 data and theoretical expectations using the

CTEQ2M parton distribution functions. The ratio of the W and Z cross-sections measured from the 1992–93 data is:

$$R = \frac{\sigma \cdot BR(W \to \ell\nu)}{\sigma \cdot BR(Z \to \ell^+\ell^-)} = 10.90 \pm 0.49 \text{ (stat} \oplus \text{syst)}. \quad (1)$$

Since many systematic errors cancel in this ratio the precision of this measurement is limited by the statistics and the expected error from the analysis of the full data set collected in 1994–1995 is ~ 2.5 times smaller than the cited one.

4.2 W width

A measurement of the W width constrains the existence of new particles produced in W decays. The width of the W was calculated using the measured ratio of W and Z cross sections times leptonic branching fractions, the value of $B(Z \to \ell^+\ell^-)$, and the theoretical calculation of σ_W/σ_Z. From these, the leptonic branching ratio of the W was calculated: $B(W \to \ell\nu) = (11.02 \pm 0.50)\%$. Using the theoretical calculation of , $(W \to \ell\nu)$ the total width of the W was calculated to be

$$, (W) = 2.044 \pm 0.093 \text{ GeV}.$$

Combining this value with other measurements gives a weighted average of , $(W) = 2.062 \pm 0.059$ GeV which is in excellent agreement with the SM prediction of 2.077 ± 0.014 GeV. Comparison of the weighted average with the SM gives a 109 MeV 95% confidence level (CL) upper limit on the width of unexpected W decays. For instance, this measurement can be used to set a direct limit on the top quark mass independent of its decay channels: $m_t >$ 61 GeV/c^2 at 95% CL. Certain limits on supersymmetric charginos and neutralinos masses can also be set.

4.3 W mass

A direct measurement of the W mass provides another crucial test of the SM. DØ uses the $p\bar{p} \to W + X \to e\nu + X$ production for the W mass measurement. Since the longitudinal momentum of neutrino can not be measured with a typical collider detector (because of particles emitted near the beam pipe and multiple interactions), the transverse mass of the $e\nu$ pair is used to infer the W mass. This quantity is less sensitive to systematic biases than the electron or missing transverse energy, which can also be used for a determination of the mass.

Since the W mass measurement is a high precision experiment, it is essential to determine the energy scale of the calorimeter correctly. We use the position of the Z-peak in order to set this scale, so in fact the m_W/m_Z ratio is measured instead of m_W. Since the Z mass is known to very high precision, such a measurement can be used to extract the W mass.

It is essential to have a fast, reliable Monte Carlo program which reproduces the detector response to the signal in order to study numerous systematics errors. A specialized code was developed using parametrizations of different resolutions measured from real data. This generator takes into account such effects as particle momenta and vertex position smearing,

transverse momentum of the W due to associated jet production, angular correlations in the decay of a polarized W, underlying event contribution, calorimeter and electronics noise, final state radiation, and parton distributions in the interacting protons and antiprotons. The reliability of the fast generator was tested extensively using the $Z \to ee$ data sample. The systematic error is dominated by the energy scale uncertainty (170 MeV). The overall systematic error is 250 MeV.

The background is dominated by QCD multijet production with mismeasured missing transverse energy and a jet passing the electron selection criteria. Other sources of the background are $Z \to ee$ decays with one electron being lost an therefore faking the missing transverse energy, and $W \to \tau\nu_\tau \to e\nu_e\bar{\nu}_\tau\nu_\tau$ decays. The total background is $\sim 2.5\%$ of the signal.

A maximum likelihood fit to the transverse mass distribution for the data from the 1992-93 run is shown in Fig. 32. The data agree well with the Monte Carlo predictions. The estimated statistical error of the fit is 140 MeV, which gives an overall uncertainty in the W mass measurement of 285 MeV (statistical and systematic errors are added in quadrature). The Monte Carlo describes both the transverse momentum of the electron and the missing transverse energy very well, as shown in Fig. 33. Performing a precision measurement at the level of 0.1% with a new detector requires extensive and careful work. Final verification of the systematic errors is progressing well and should be completed soon.

Since most of the systematic errors are determined from the $Z \to ee$ sample, they are dominated by the available Z statistics. Therefore, both systematic and statistical errors are expected to decrease by a factor of 2.5 with the analysis of the larger 1994–95 sample. The expected uncertainty in the W mass measurement from this analysis is $\sim$ 100 MeV.

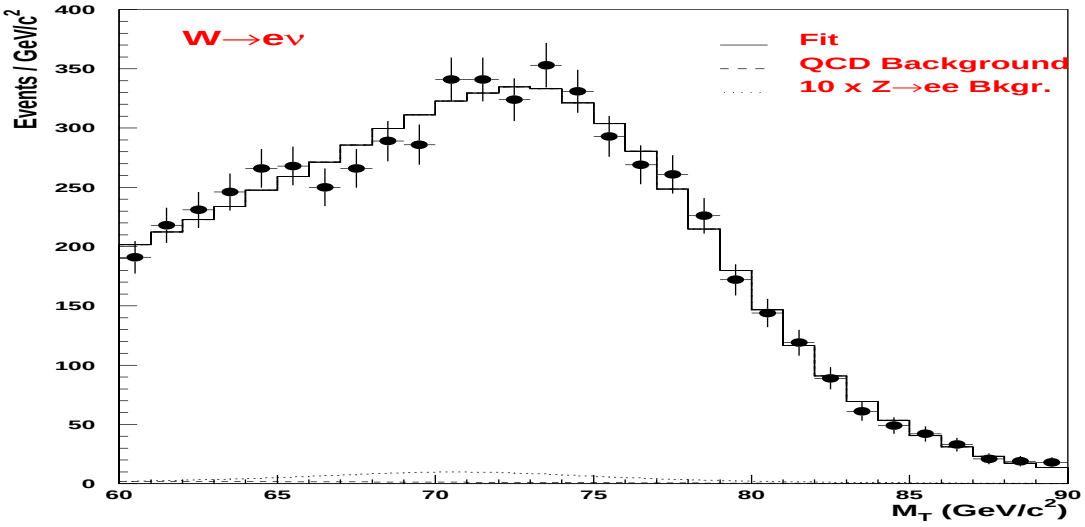

Figure 32: Fit to the transverse mass of the $W \to e\nu$ candidates. Points represent the data, the dashed and dotted lines represent estimated backgrounds, the solid histogram shows the best fit to signal plus background with the W mass being a free parameter.

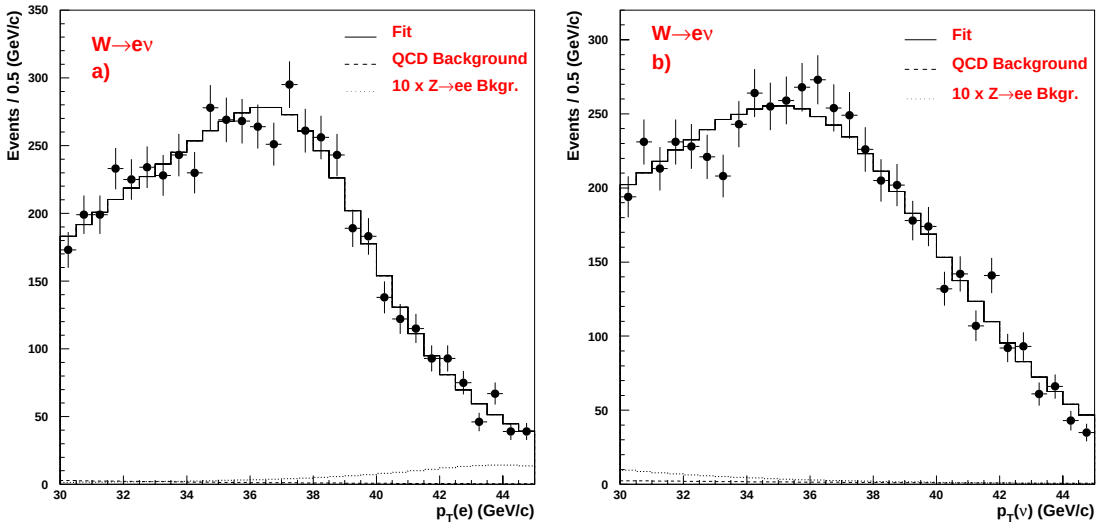

Figure 33: (a) Transverse momentum of the electron. Points represent the data, the dashed and dotted lines show estimated backgrounds, the solid histogram represents the best fit for signal plus background with the W mass being a free parameter. (b) The same for the missing transverse energy.

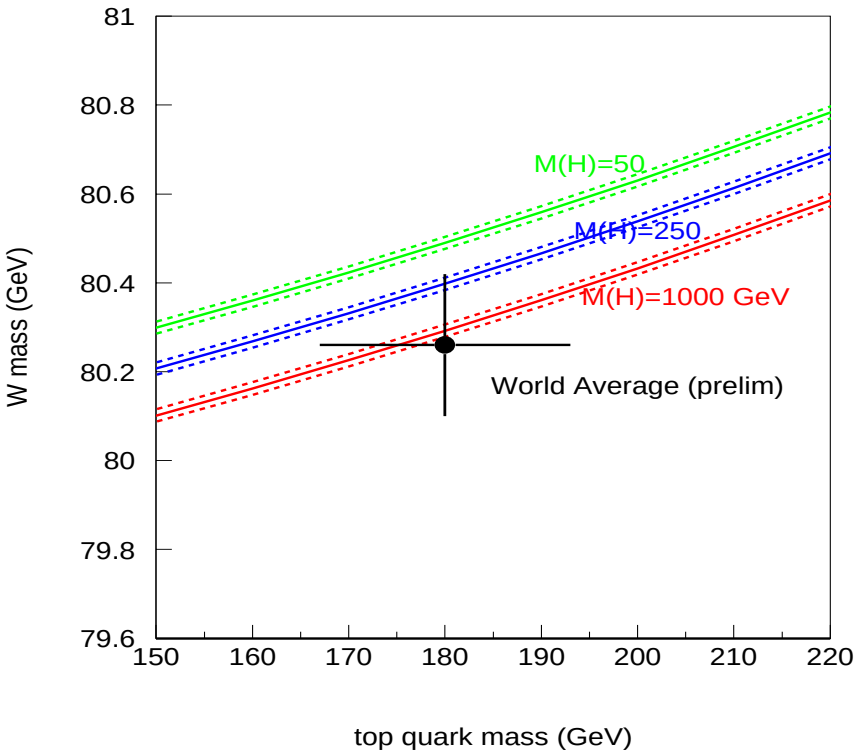

Figure 34: W mass vs. t-quark mass plane. Solid lines are the SM predictions for Higgs masses of 50, 250, and 1000 GeV with their errors (dashed bands). The point shows the world averages for the W and top masses.

4.4 Electroweak constraints on the Higgs mass

An important constraint on the mass of the Higgs boson (H^0), can be obtained from the radiative corrections to the W and Z masses via heavy quark and H^0 virtual loops. The "tree-level" mass prediction of the SM W boson can be inferred from the three SM parameters, α, G_F, and m_Z, that are measured to a very high precision. It is further modified by inclusion of radiative corrections. The contribution of the top-quark loop to the W mass is proportional to m_t^2, and that for the Higgs boson loop behaves like $\log m_H$ in the limit of heavy top and Higgs particles. A direct measurement of the W mass, therefore, can determine the size of the corrections and, given a top mass measurement, impose constraints on the Higgs mass.

Figure 34 shows the world average for the W and top masses in the m_t–m_W plane. Shown with the solid lines are the SM predictions for different Higgs masses. Even though the measurement combinederrors are quite large in both directions in this plane, it appears that these two pieces of data prefer heavy Higgs. It is essential to reduce the errors on m_t and especially on m_W measurements. The DØ W mass measurement and improved top mass determination will help here. In the near term, both m_t and m_W precision will be improved (to about 100 MeV and 10 GeV respectively) using the 1994-95 data set. Further progress on this central issue for particle physics will be possible with the much larger data samples of the Main Injector era, and the upgraded DØ detector.

4.5 Diboson production

A central feature of the SM electroweak model is the self-couplings of the W, Z, and γ bosons, and thus a well-defined prediction of gauge boson pair production. Theoretical studies of this subject started about 20 years ago and the calculations exist now for all possible pairs. $W\gamma$, $Z\gamma$, WW and possibly WZ production can be studied at Tevatron energies with present luminosities, however the ZZ production cross section is extremely small. DØ has studied these processes extensively, and several papers on this subject have recently been published.

In the SM, pair production of the gauge bosons arises either from the t-channel quark exchange diagrams or from the direct s-channel diagram with a third vector boson as a mediating particle. The latter process is described by the trilinear vector boson couplings which are fixed in the SM. Direct measurement of these couplings provides sensitive tests of the SM gauge sector, since any deviation from the SM predictions would imply new physics. Furthermore, the non-SM (or *anomalous*) values of the trilinear couplings increase the cross section of the corresponding pair production, which gives an experimentally favorable signature. The anomalous couplings generally result in high-p_T enhancements of vector boson production. For the $WW\gamma$ vertex, non-SM values of couplings can be interpreted as anomalous electromagnetic dipole and quadrupole moments of the W; for $ZZ\gamma$ and $Z\gamma\gamma$ couplings they correspond to anomalous electromagnetic transition moments.

Generally, each trilinear vertex can be described by a set of four coupling constants. The $WW\gamma$ (WWZ) couplings are usually referred to as $\kappa_{\gamma(Z)}$, $\lambda_{\gamma(Z)}$, $\tilde{\kappa}_{\gamma(Z)}$, $\tilde{\lambda}_{\gamma(Z)}$, with the first two couplings being CP-conserving and the other two being CP-violating. For $ZZ\gamma$ ($Z\gamma\gamma$) vertices the corresponding couplings are denoted $h_i^{Z(\gamma)}$, $i = 1...4$ with $h_{1,2}$ being CP-violating and $h_{3,4}$ CP-conserving. In order to respect the S-matrix unitarity one has to

modify the couplings with energy dependent form-factors with the energy scale Λ being a probe of the mass scale of new physics which gives rise to the anomalous couplings. Only the $\kappa_{\gamma,Z}$ couplings are non-zero in the SM (they are equal to one); all others are fixed at zero by the non-Abelian gauge invariance of the SM Lagrangian. The following notation will be therefore used throughout this section: $\Delta\kappa = \kappa - 1 (= 0$ in SM).

DØ has completed the analyses of the $W\gamma$, $Z\gamma$ and WW pair production in the electron and muon decay modes of W and Z, as well as the study of the WW, WZ production in the $e\nu jj$ decay mode (one W decaying in electron channel, and the other W or the Z decaying hadronically). The analysis of the experimentally challenging $Z\gamma \rightarrow \nu\nu\gamma$ decay mode is currently in progress.

The lepton channel results are based on the 1992–1993 data run. We observe 23 $W\gamma$, 6 $Z\gamma$, and 1 WW candidates in electron and muon channels combined. The backgrounds in these channels are dominated by the single vector boson production with associated jets and the "leakage" between the channels due to the mis-reconstructed final state particles. The total backgrounds are 6.4 ± 1.4, 0.48 ± 0.06, and 0.56 ± 0.13 events respectively. The E_T spectra of the photon in the $(W/Z)\gamma$ production are shown in Figs. 35 and 36 and exhibit good agreement with the SM predictions.

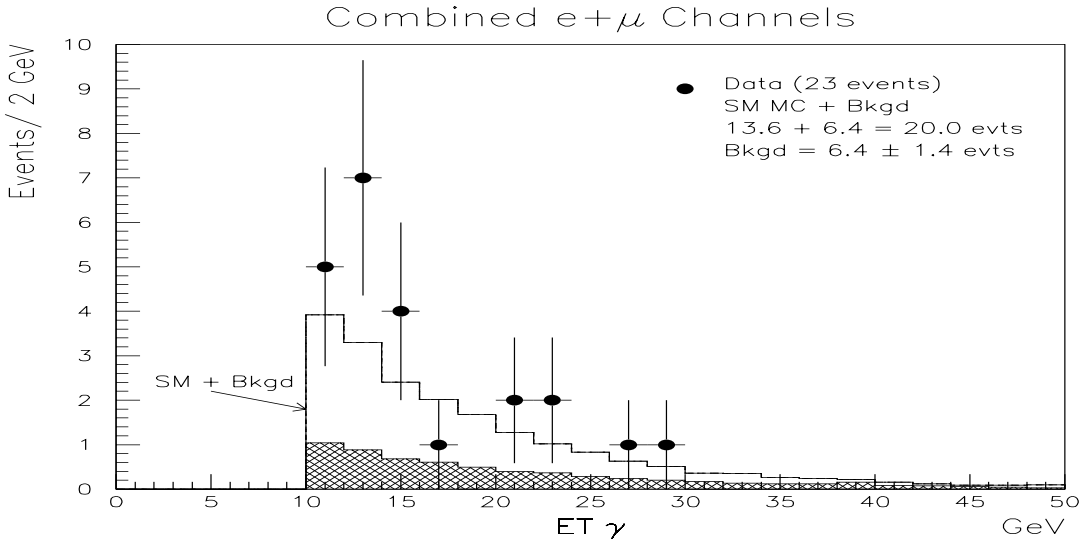

Figure 35: Transverse energy spectrum of the photon produced in $p\bar{p} \rightarrow W\gamma + X \rightarrow \ell\nu\gamma + X$, $\ell = e, \mu$. The points are data, the shaded area represents the estimated background, and the solid histogram is the sum of the SM prediction and estimated background.

The shapes of the photon transverse energy spectra in Figs. 35 and 36 were used to set limits on the anomalous $WW\gamma$, $ZZ\gamma$ and $Z\gamma\gamma$ couplings. The spectra were fit to the sum of the expected background and anomalous production. A binned likelihood method was used during the fit. Errors on the efficiencies and integrated luminosities were properly taken into account. The fits of both spectra prefer the SM couplings. The 68% and 95% confidence level limits are shown in Figs. 37 and 38. The latter plot shows the $ZZ\gamma$ coupling limits; the corresponding $Z\gamma\gamma$ limits are the same within 5%. Figure 37(b) explicitly shows the relation between anomalous couplings and multipole electromagnetic moments of the W boson. For instance, the point indicated by the star, which corresponds to $U(1)_{\mathrm{EM-only}}$

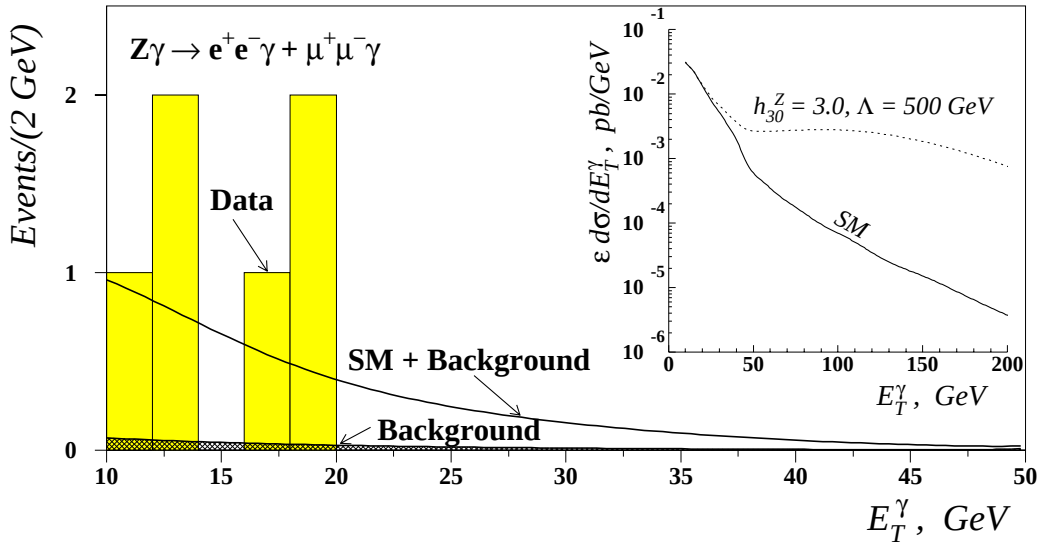

Figure 36: Transverse energy spectrum of the photon produced in $p\bar{p} \to Z\gamma X \to \ell^+\ell^-\gamma X$, $\ell = e, \mu$. The histogram is data, the shaded area represents the estimated background, the solid line is the sum of the SM prediction and estimated background. The insert shows the differential cross sections $d\sigma/dE_T^\gamma$ for the SM and the anomalous coupling ($h_3^Z = 3$) cases.

values of the electric quadrupole moment and magnetic dipole moment (gyromagnetic ratio $g_W = 1$), is excluded by this measurement at 80% CL. Therefore DØ has indeed observed the "anomalous" (non-classical) magnetic dipole moment of the W which is a direct consequence of the gauge invariance of the non-Abelian $SU(2)$ part of the SM Lagrangian.

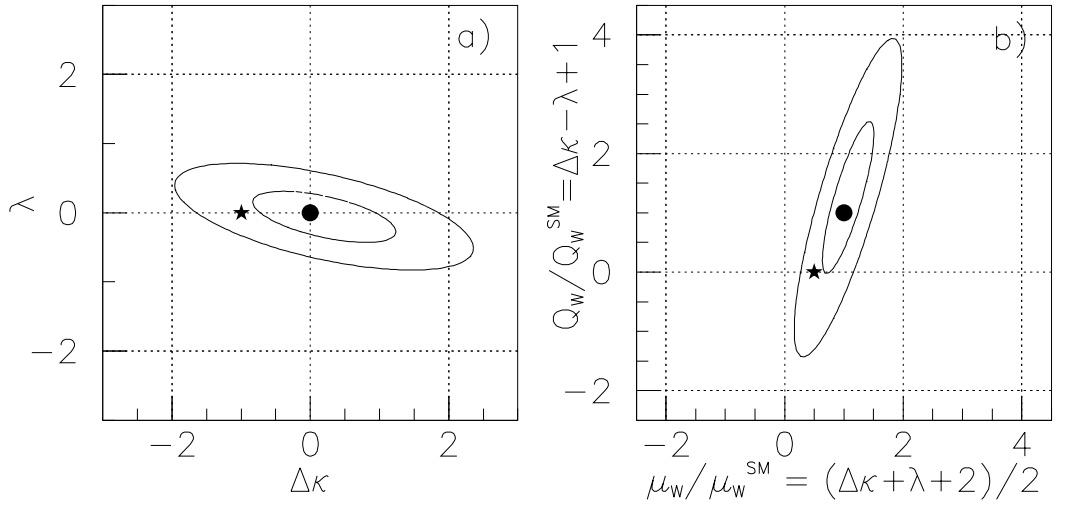

Figure 37: Limits on (a) CP-conserving anomalous coupling parameters $\Delta\kappa$ and λ, and on (b) the magnetic dipole μ_W and electric quadrupole Q_W^e moments of the W boson. The ellipses represent the 68% and 95% CL exclusion contours. The dot represents the SM values, while the star indicates the $U(1)_{\mathrm{EM-only}}$ coupling of the W boson to a photon. Form-factor scale $\Lambda = 1.5$ TeV.

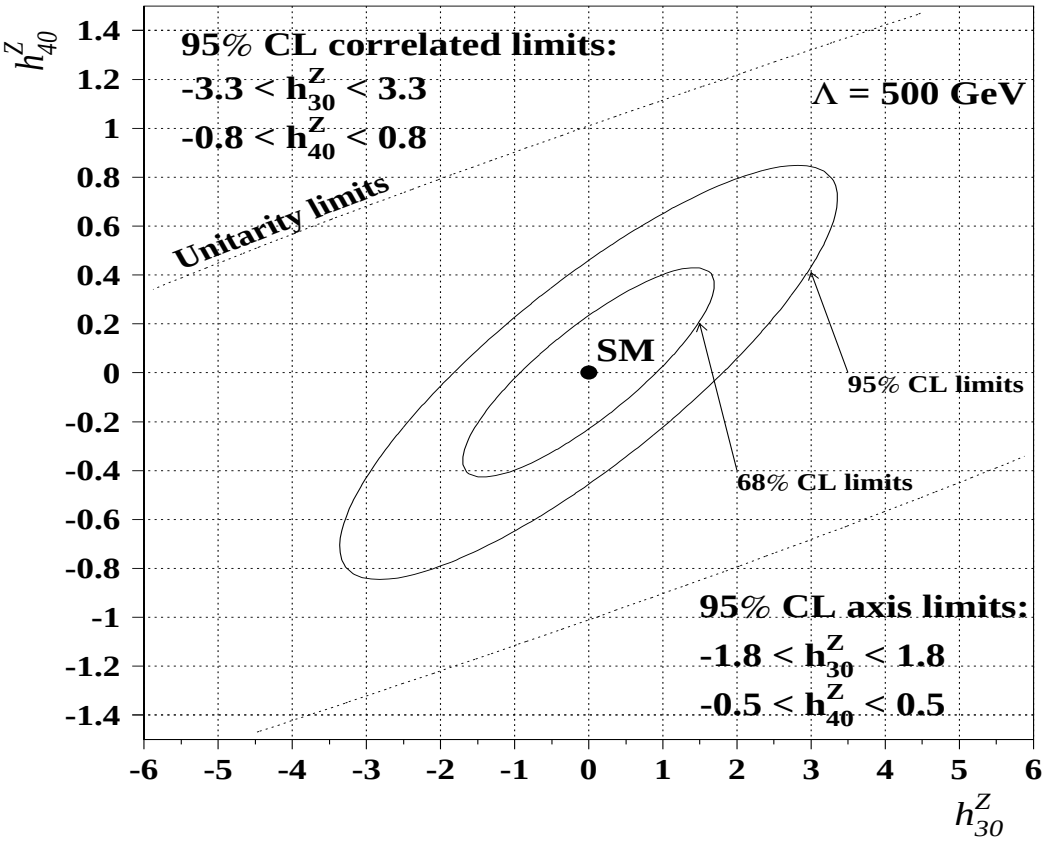

Figure 38: Limits on the CP-conserving anomalous $ZZ\gamma$ couplings h_{30}^Z and h_{40}^Z. The ellipses represent 68% and 95% CL exclusion contours. The dashed line shows the S-matrix unitarity limits. Form-factor scale $\Lambda = 500$ GeV.

Anomalous couplings would increase the WW cross section over that of the standard model. Since only one event was observed in the $WW \to \ell^+\ell^-\nu\nu$ mode, this is not observed and we set limits on non-SM couplings. The limits, assuming $\Delta\kappa_\gamma = \Delta\kappa_Z$ and $\lambda_\gamma = \lambda_Z$, are shown in Fig. 39. The limits are inside the region allowed by the S-matrix unitarity for the values of the form-factor $\Lambda < 900$ GeV.

For the $WW/WZ \to e\nu jj$ analysis, the transverse momentum of the W decaying leptonically is shown in Fig. 40(a). At low transverse momentum it is dominated by the background from $W+ \geq 2j$ production, as is shown with a dotted line in this figure. The total background (dashed line) includes an additional contribution from QCD multijet production (significant at low transverse momenta). The observed data (points) are consistent with the background. The SM prediction for WW/WZ production in this channel is shown in Fig. 40(b) with a dotted line, and it is negligible compared to the background. The anomalous couplings, however, produce a significant tail at high transverse momenta clearly different from the background shape (dashed line in the same figure).

Limits on the anomalous $WW\gamma$, WWZ couplings in the $WW \to e\nu jj$ channel are obtained by fitting the p_T^W spectrum (Fig. 40), just as in the $(W/Z)\gamma$ case. They are shown in Fig. 41. Here the exclusion contours are within the unitarity limits for the form-factor scales up to 1.5 TeV.

Limits on the CP-violating couplings for all these four measurements are numerically

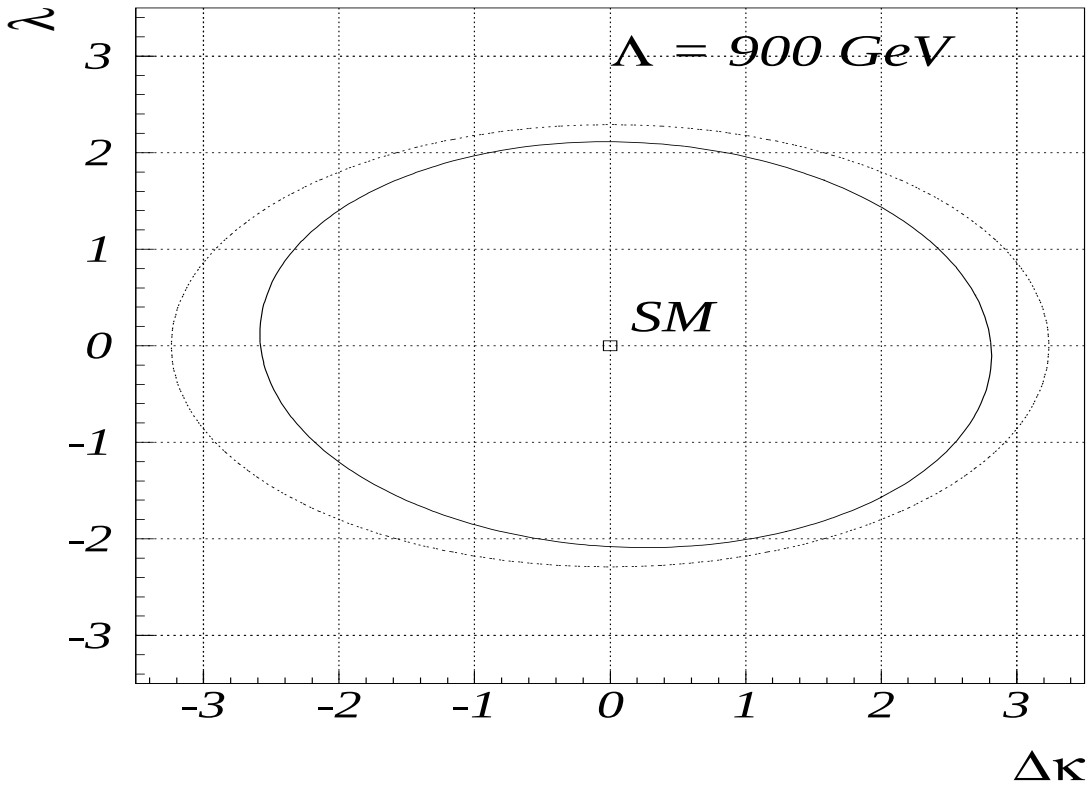

Figure 39: 95% CL limits on the *CP*-conserving anomalous couplings $\Delta\kappa$, λ assuming $\Delta\kappa_\gamma = \Delta\kappa_Z; \lambda_\gamma = \lambda_Z$ derived from $WW \to \ell^+\ell^-\nu\nu$. The dashed line shows the S-matrix unitarity limits. Form-factor scale $\Lambda = 900$ GeV.

CP-conserving coupling limits		Channel
$-1.6 < \Delta\kappa_\gamma < 1.8,$	$-0.6 < \lambda_\gamma < 0.6$	($W\gamma$, $\Lambda = 1500$ GeV)
$-1.8 < h^Z_{30} < 1.8,$	$-0.5 < h^Z_{40} < 0.5$	($Z\gamma$, $\Lambda = 500$ GeV)
$-1.9 < h^\gamma_{30} < 1.9,$	$-0.5 < h^\gamma_{40} < 0.5$	($Z\gamma$, $\Lambda = 500$ GeV)
$-2.6 < \Delta\kappa_\gamma = \Delta\kappa_Z < 2.8,$	$-2.1 < \lambda_\gamma = \lambda_Z < 2.1$	($WW \to \ell^+\ell^-\nu\nu$, $\Lambda = 900$ GeV)
$-0.9 < \Delta\kappa_\gamma = \Delta\kappa_Z < 1.1,$	$-0.7 < \lambda_\gamma = \lambda_Z < 0.7$	($WW/WZ \to e\nu jj$, $\Lambda = 1500$ GeV)

Table 2: Limits on the *CP*-conserving couplings. Limits for the *CP*-violating couplings are the same within 5%.

the same as those shown for the *CP*-conserving ones. The numerical limits on the different couplings when only one coupling varies at a time are summarized in Table 2.

A 50% improvement on these limits is expected with the analysis of the 1994–1995 run. Figure 42 shows, as an example, the E_T^γ spectrum for $p\bar{p} \to W\gamma + X \to e\nu\gamma + X$ for about 70% of the new data set. The data are in good agreement with the SM predictions plus the estimated background.

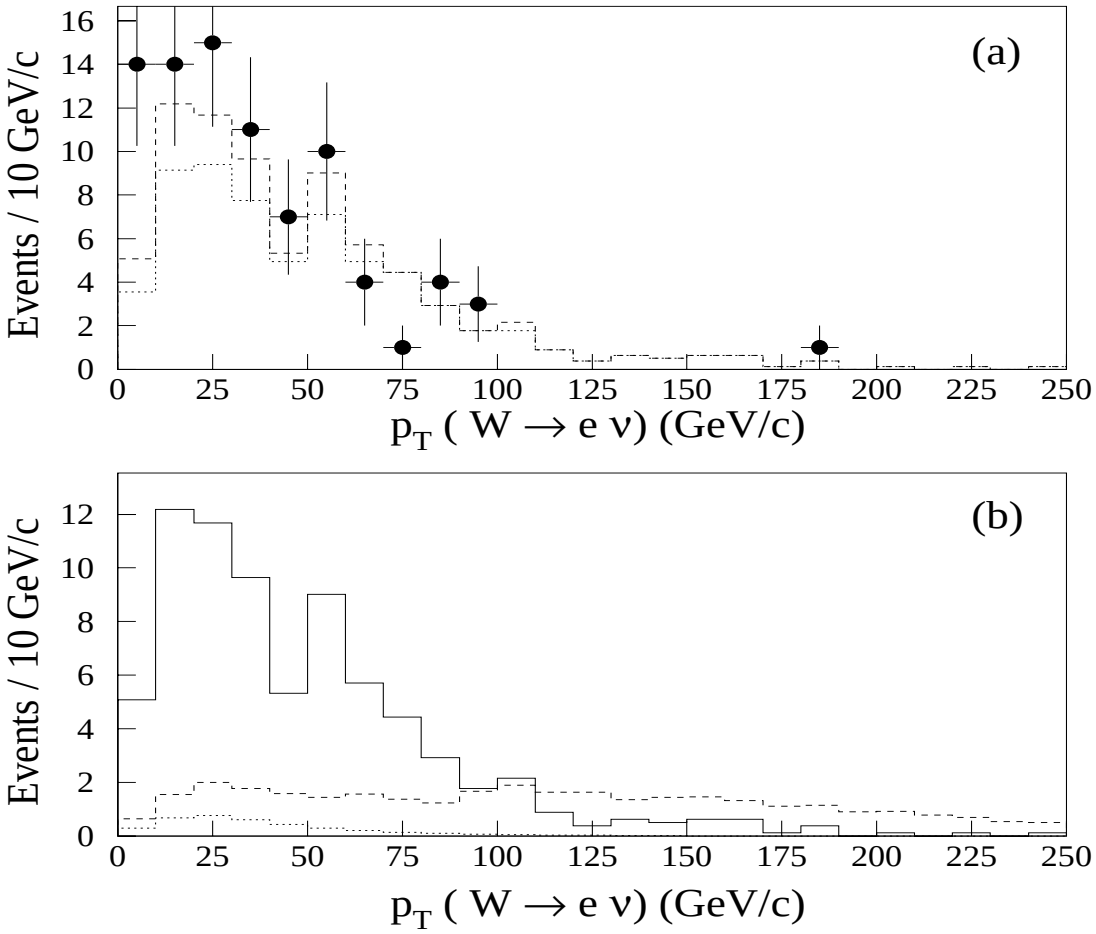

Figure 40: Transverse momentum spectrum of the $e\nu$ system: (a) data (points), $W+ \geq 2j$ background (dotted), total background (dashed); (b) the total background above (solid), Monte Carlo predictions for the SM (dotted) and anomalous (dashed, $\Delta\kappa_Z = \Delta\kappa_\gamma = 2, \lambda_Z = \lambda_\gamma = 1.5$) WW production.

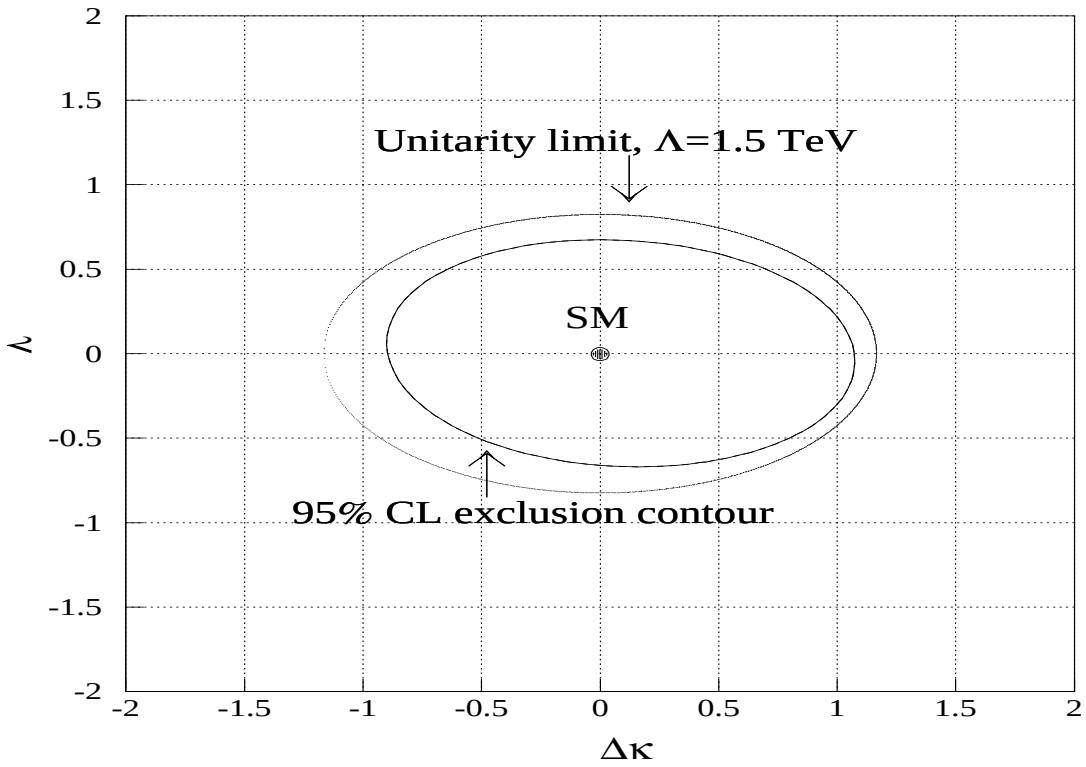

Figure 41: 95% CL limits on the *CP*-conserving anomalous couplings $\Delta\kappa$, λ assuming $\Delta\kappa_\gamma = \Delta\kappa_Z; \lambda_\gamma = \lambda_Z$ derived from $WW/WZ \to e\nu jj$. The dashed line shows the S-matrix unitarity limits. Form-factor scale $\Lambda = 1500$ GeV.

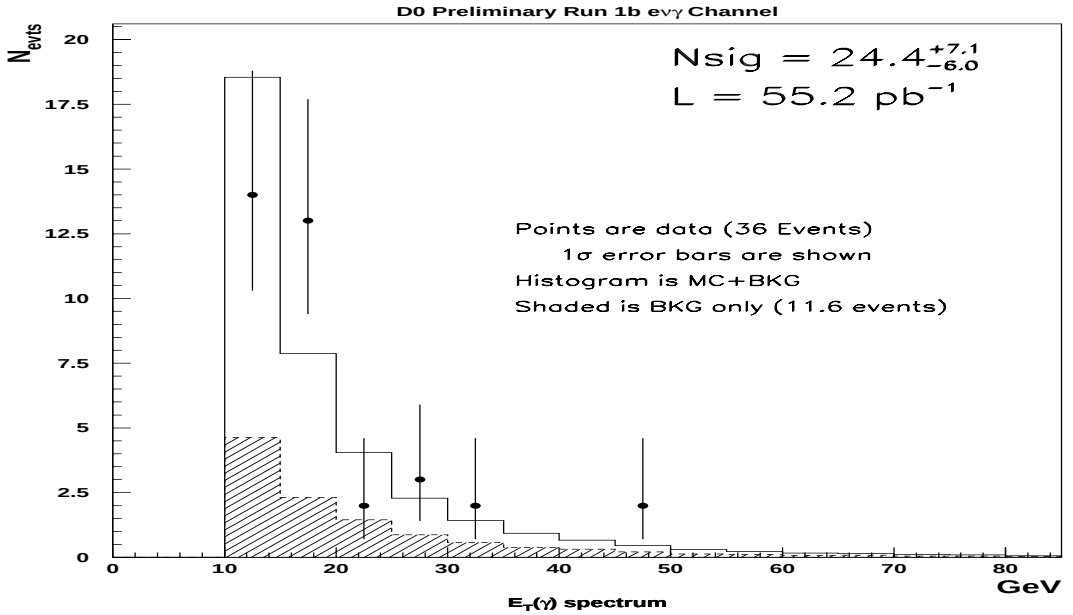

Figure 42: Photon transverse energy spectrum for $W\gamma \to e\nu\gamma$ data from $\approx 70\%$ of the 1994–95 data statistics. The points show the data with Poisson errors, the hatched histogram represents the background estimate, and the open histogram shows the background plus SM signal expectation.

5 Beyond the Standard Model

There are many theoretical prejudices against the standard model: there are nineteen free parameters, the choice of the $SU(3)_c \times SU(2)_L \times U(1)_Y$ gauge group is *ad hoc*, breaking of the electroweak symmetry introduces the only fundamental scalar in the theory, whose mass must be carefully fine-tuned. Many physicists feel the standard model is a low energy approximation of a more fundamental theory – a Grand Unified Theory (GUT) which unifies the three interactions of the the standard model at some very high energy scale. There are many candidate GUT's including technicolor, supersymmetry (SUSY), left-right symmetric models, and composite models which postulate more fundamental states which make up quarks and leptons. In looking for new particles, we search for some hint as to which, if any, of these theoretical models holds the correct description of nature.

5.1 SUSY Searches

Supersymmetric extensions of the standard model, which relate bosons and fermions, are especially attractive because they remove the so called fine-tuning problem associated with loop corrections to the mass of the Higgs boson. A new array of particle states is introduced. These supersymmetric partners (or "sparticles") of the particles of the standard model are summarized in Table 3; this particular complement of sparticles is usually referred to as the *Minimal Supersymmetric Standard Model* (MSSM).

Every particle or sparticle carries a SUSY "charge", called *R-parity*. If R-parity is conserved, then sparticle states are produced in pairs. Unstable sparticles must decay into a lighter sparticle (plus other ordinary particles); there must then be one sparticle which does not decay. This is referred to as the *Lightest Supersymmetric Particle* (LSP). The only candidates for the LSP in the MSSM are the $\tilde{\nu}$ and the $\tilde{Z}_1$. Most models which conform to previous experimental limits have the $\tilde{Z}_1$ as the LSP.

The data on the running of the coupling constants published by the LEP experiments suggest that the couplings do not meet at a common unification scale. However, the second order renormalization group equations of the MSSM are consistent with such a unification of the couplings. This is an enticement to search for evidence of SUSY particles.

5.1.1 Squarks and Gluinos

At the Tevatron the most copiously produced SUSY particles would be squarks ($\tilde{q}$) and gluinos ($\tilde{g}$). In previous searches, the $\tilde{q}$ and $\tilde{g}$ were assumed to decay directly into quarks and the lightest supersymmetric particle. For heavier squarks and gluinos ($\mathcal{O}(100$ GeV/c$^2)$) the $\tilde{q}$ and $\tilde{g}$ decay through a cascade of neutralinos $\tilde{Z}_1 ... \tilde{Z}_4$ and charginos $\widetilde{W}_1$,$\widetilde{W}_2$ to a final state containing quarks, possibly leptons, and the LSP. The event signature for which we have searched is three or more jets and missing transverse energy ($\not\!\!E_T$). We have conducted two searches: one which searched for events with three or more high E_T jets and very large $\not\!\!E_T$, and another where events were required to have at least four jets but slightly less $\not\!\!E_T$.

The major backgrounds to these searches are vector boson production with associated jets and QCD events with mismeasured jet energies. After analysis cuts, 14 events survived in the three jet analysis and 5 events in the four jet sample.

Standard Model States		SUSY Partners	
Particle name	Symbol	Sparticle name	Symbol
quark	q	squark	$\tilde{q}_L$, $\tilde{q}_R$
lepton	l	slepton	$\tilde{l}_L$, $\tilde{l}_R$
neutrino	ν	sneutrino	$\tilde{\nu}$
gluon	g	gluino	$\tilde{g}$
charged Higgs	$H^{\pm}$	chargino	
charged weak boson	W	("wino")	$\tilde{W}_i$, i=1,2
light Higgs	h		
heavy Higgs	H	neutralino	
pseudoscalar Higgs	A	("zino")	$\tilde{Z}_i$, i=1-4
neutral weak boson	Z		
photon	γ		

Table 3: The (s)particle content of the Minimal Supersymmetric Standard Model.

Backgrounds from vector bosons plus jets backgrounds were estimated with the VECBOS Monte Carlo generator utilizing ISAJET to hadronize final partons and supply the underlying event. The detector response was simulated using the DØGEANT detector simulation program. A total of 14.2 ± 4.4 W/Z events are expected to pass the three jet analysis cuts. For the four jet search, 5.5 ± 2.2 events are predicted.

The contribution from multijet production was estimated using data from jet triggers. We predict 0.42 ± 0.37 events for the three jet analysis and 1.6 ± 0.9 events for the four jet search.

The number of events seen in the squark/gluino data sample is consistent with these standard model backgrounds and thus no signal is observed. The results of the search are not very sensitive to the choice of charged Higgs mass nor to the top quark mass. We determine the 95% confidence limit contour in the $m_{\tilde{g}}$–$m_{\tilde{q}}$ mass plane shown in Fig. 43. The three jet analysis is more sensitive for small squark mass (below approximately 220 GeV/c^2), while the four jet analysis is the most sensitive for larger squark mass. Combining the two searches yields a preliminary 95% CL lower mass limit of $m_{\tilde{g}} > 173$ GeV/c^2 for large squark mass and a lower mass limit of $m > 229$ GeV/c^2 for the case of equal mass squarks and gluinos.

5.1.2 The Top Squark

The squark/gluino searches assumed that the squarks are mass degenerate, a common feature of SUSY models with a common scalar mass at the GUT scale. However, we now know that the top quark is heavy. The large top mass can drive the mass of its SUSY partner, the top squark or stop ($\tilde{t}$) to lower masses than the other squark. Mixing between the left- and right-handed top squarks can also leave one of the two $\tilde{t}$ lighter than the top quark itself. A very light top squark could modify the top decays as well as producing additional backgrounds to the top cross section measurement. A light top squark mass is popular in light of recent

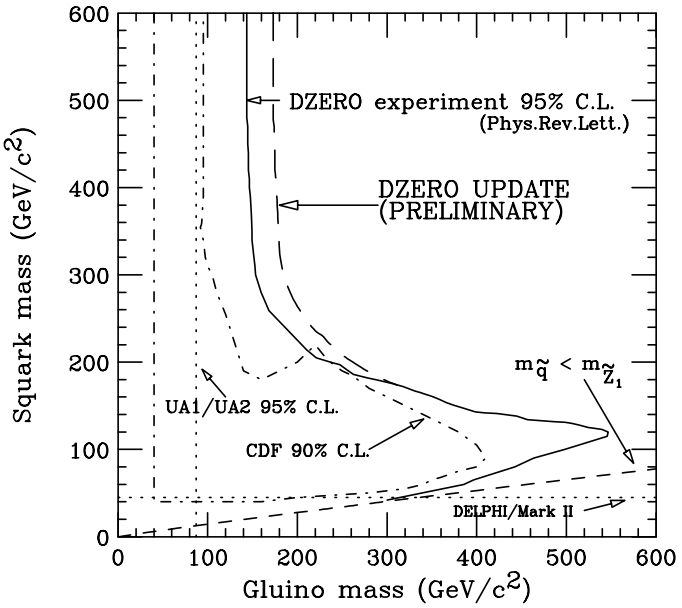

Figure 43: The squark and gluino mass limits. The long dashed line marks the *preliminary* DØ 95% confidence level excluded region from the combination of the three jet and four jet analyses. The solid line indicates the DØ three jet search result. The region below the dashed line labeled $m_{\tilde{q}} < m_{\tilde{Z}_1}$ is excluded since there the squark becomes lighter than the LSP. Other published limits from CDF, UA1, UA2, and DELPHI are displayed as well.

measurements of the $Z \to b\bar{b}$ branching fraction at LEP.

The top squark is expected to decay via $\tilde{t}_1 \to b\tilde{W}_1$. However if $m_{\tilde{W}_1} > m_{\tilde{t}_1} + m_b$ the three-body decays $\tilde{t}_1 \to bl\tilde{\nu}$ and $\tilde{t}_1 \to b\nu\tilde{l}$ will predominate *unless* sleptons and sneutrinos are also much heavier than the $\tilde{t}_1$. In this case the top squark will decay via $\tilde{t}_1 \to c\tilde{Z}_1$ producing final states with two acollinear jets and $\not\!\!E_T$. In either case, the expected signature of the top squark events is two energetic jets and large $\not\!\!E_T$ from the two LSP's.

While the top squark production occurs via gluon fusion and $q\bar{q}$ annihilation and is thus fixed by QCD in terms of $m_{\tilde{t}_1}$, its decay topology is solely determined by $m_{\tilde{t}_1}$ and $m_{\tilde{Z}_1}$. The search for the top squark is then over a two–parameter space in $m_{\tilde{Z}_1}$ *vs.* $m_{\tilde{t}_1}$. Our background subtracted 95% CL exclusion limit contour is shown in Fig. 44. This contour intersects the $m_{\tilde{t}_1} = m_{\tilde{\chi}_1^0} + m_b + m_W$ line at $m_{\tilde{Z}_1} = 8$ GeV/c^2 and $m_{\tilde{t}_1} = 93$ GeV/c^2, the highest $m_{\tilde{t}_1}$ value we exclude. The maximum excluded value for $m_{\tilde{Z}_1}$ is 44 GeV/c^2 for $m_{\tilde{t}_1} =$ 85 GeV/c^2.

5.1.3 Gaugino Searches

Another class of SUSY searches of interest at the Tevatron is the search for gaugino partners of the W and Z bosons. Over the past few years, theorists have shown that the cross section for producing chargino and neutralino pairs at the Tevatron could be significant. The largest production cross section is into a $\widetilde{W}_1\widetilde{Z}_2$ pair. The decays of the $\widetilde{W}_1$ and $\widetilde{Z}_2$ can lead to final states similar to those from off-mass shell W and Z bosons plus missing E_T from the LSP's. Thus the possible event signatures are: 1) Four jets + $\not\!\!E_T$, 2) Lepton + Two Jets + $\not\!\!E_T$,

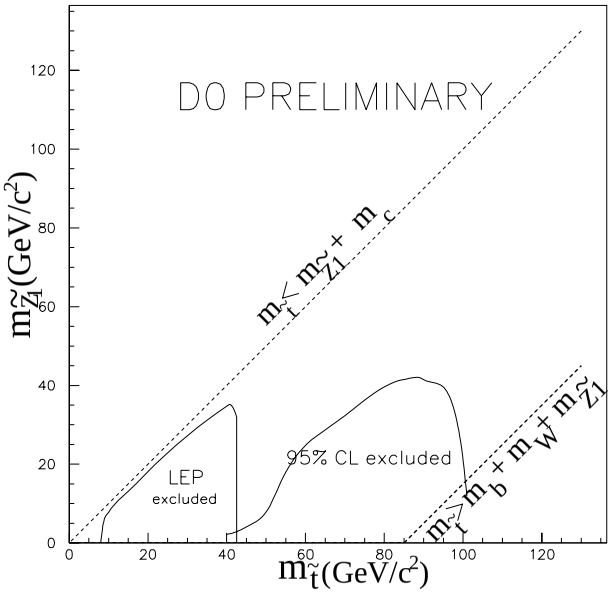

Figure 44: The DØ 95% Confidence Level top squark exclusion contour. Also shown is the result from LEP (OPAL experiment).

3) Two Leptons + Two Jets + $\not\!\!E_T$, and 4) Three Leptons + $\not\!\!E_T$. The last channel has few standard model backgrounds and is relatively clean in terms of hadronic activity. DØ has searched for this trilepton final state and produced limits on $\sigma(\widetilde{W}_1\widetilde{Z}_2) \cdot BR$ for the process $p\bar{p} \rightarrow 3\ell + X$. We see no candidate events consistent with $\widetilde{W}_1\widetilde{Z}_2$ pair production and subsequent decay into trilepton final states.

Detection efficiencies were determined using a combination of data and Monte Carlo simulations. Monte Carlo signal events were generated using ISAJET and a full simulation of the DØ detector based on the GEANT program. The value of the gluino mass in ISAJET was varied from 160 to 355 GeV/c^2 to generate the corresponding $\widetilde{W}_1$ masses from 45 to 100 GeV/c^2. For these events, $m_{\widetilde{W}_1} \approx m_{\widetilde{Z}_2} \approx 2 \times m_{\widetilde{Z}_1}$, so that efficiencies can be parameterized as a function of $m_{\widetilde{W}_1}$. These Monte Carlo events were used to determine kinematic and geometric acceptances only.

The primary sources of background are single lepton and dilepton events with one or more misidentified leptons. These are estimated from data whenever possible, supplemented with Monte Carlo simulations.

Based on zero candidate events, we present a 95% confidence level upper limit on the cross section for producing $\widetilde{W}_1\widetilde{Z}_2$ pairs times the branching ratio into any trilepton final state. The results from the four channels were combined in the calculation of the limit, with the assumption that $BR(eee) = BR(ee\mu) = BR(e\mu\mu) = BR(\mu\mu\mu)$. In calculating the limit we used the Bayesian approach, with the distribution of systematic errors represented by Gaussians and a flat prior distribution for the signal cross section.

In Fig. 45 we show the resulting limit in the region above the LEP limit. For comparison, we show three bands of theoretical curves. Band (a) shows the ISAJET production cross

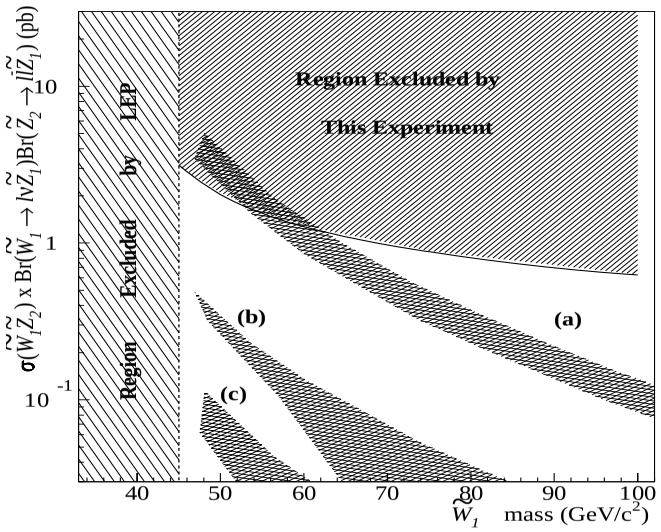

Figure 45: The 95% CL limit on cross section times branching ratio into any one trilepton final state, as a function of $m_{\widetilde{W}_1}$, along with the region of $m_{\widetilde{W}_1}$ excluded by LEP. Also shown are bands of theoretical predictions, as described in the text.

section obtained with a wide range of input parameters, multiplied by a branching ratio of $\frac{1}{9}$. The value of $\frac{1}{9}$ for a single trilepton channel is obtained when the $\widetilde{W}_1$ and $\tilde{Z}_2$ decay purely leptonically and lepton universality is applied. Branching ratios of this order are predicted in models with very light sleptons. Bands (b) and (c) show the $\sigma \cdot BR$ values from ISAJET obtained with $m_0 = [200, 900]$GeV/c^2, $m_{\frac{1}{2}} = [50, 120]$GeV/c^2, $A_0 = 0$ and the sign of μ negative. Band (b) is for $\tan\beta = 2$ and band (c) for $\tan\beta = 4$.

5.1.4 The Bosonic Higgs

The outstanding missing piece of the standard model, with the discovery of the top quark, is the Higgs boson. In the SM, one scalar Higgs field is responsible for electroweak symmetry breaking resulting in the generation of vector boson masses. It is also responsible for flavor symmetry breaking through the generation of fermion masses. Detection of the SM Higgs is difficult at the Tevatron. However DØ has searched for one particular non-SM Higgs; namely a "bosonic" Higgs which is responsible for electroweak symmetry breaking but which has little (or nothing) to do with flavor symmetry breaking. Such a Higgs would have SM coupling strengths to the vector boson, including the photon, but suppressed couplings to fermions. At the Tevatron this bosonic Higgs would be produced predominantly in association with a W or Z boson, resulting in final states in which $W/Z \to$ two jets and $H \to \gamma\gamma$ for $m_H < 90$ GeV/c^2.

DØ has searched for a bosonic Higgs in the 1992–93 data, by searching for resonances in the photon-photon invariant mass spectrum. Candidates had two high E_T photons and two jets. The invariant mass region near m_Z was excluded to remove backgrounds from $Z \to ee$ where both electrons were misidentified as photons. After all selection cuts, one event was found with $m_{\gamma\gamma} = 60$ GeV/c^2, and none in the region of higher invariant mass. Figure 46 shows the 90% CL upper limit on the mass of the bosonic Higgs, along with the expected

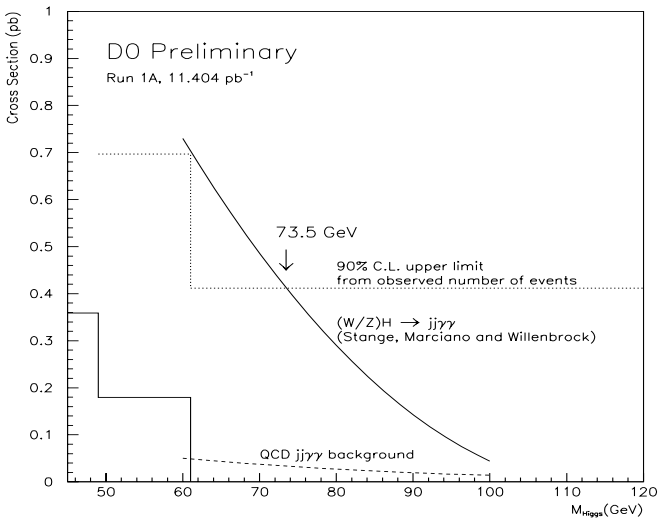

Figure 46: The 90% CL limit on the production of a bosonic Higgs.

QCD $jj\gamma\gamma$ background, and the theoretical prediction for $(W/Z)H \rightarrow jj\gamma\gamma$ production. Based on this prediction, we exclude bosonic Higgs of mass less than 73.5 GeV/c^2, at the 90% confidence level.

5.2 Heavy Gauge Boson Searches

Supersymmetry is not the only possible extension to the standard model, nor are SUSY searches the only new phenomena analyses in which DØ engages. Among the alternatives to SUSY as extensions to the SM are theories with extended gauge sectors. These theories often predict new gauge bosons, heavier counterparts to the W and Z vector bosons of the SM. DØ has searched for heavy gauge bosons in both the single lepton and dilepton final states. Additionally, so called left-right symmetric theories predict new right-handed gauge bosons and neutrinos.

In the searches for a new heavy W boson, the mass and nature of the right-handed neutrino are parameters of the model. We will first consider the search for for a heavy W' which decays into an electron and a light stable neutrino. The transverse mass distribution, $M_T^{e\nu}$, of events with a high p_T electron would show new structure not explained by standard W boson production or QCD events in which a jet is misidentified as an electron.

The M_T distribution for W candidates is shown in Fig. 47(a). The shaded portion indicates the estimated amount of QCD background events in which a jet has been misidentified as an electron and $\not\!\!E_T$ results from mismeasured energy. The contribution from standard W boson production is estimated from PYTHIA Monte Carlo and simulation of the DØ detector. The sum of W boson production and misidentified QCD events, which reproduces the data spectrum well. The upper limit on the cross section for W' boson production is calculated using a binned likelihood method with Poisson statistics to estimate the contribution of W' boson production. Fig. 47(b) shows the resulting upper limit on the cross section times branching fraction at the 95% confidence level and the theoretical cross section, assuming SM couplings, as a function of W' mass. A W' with the same couplings to quarks and

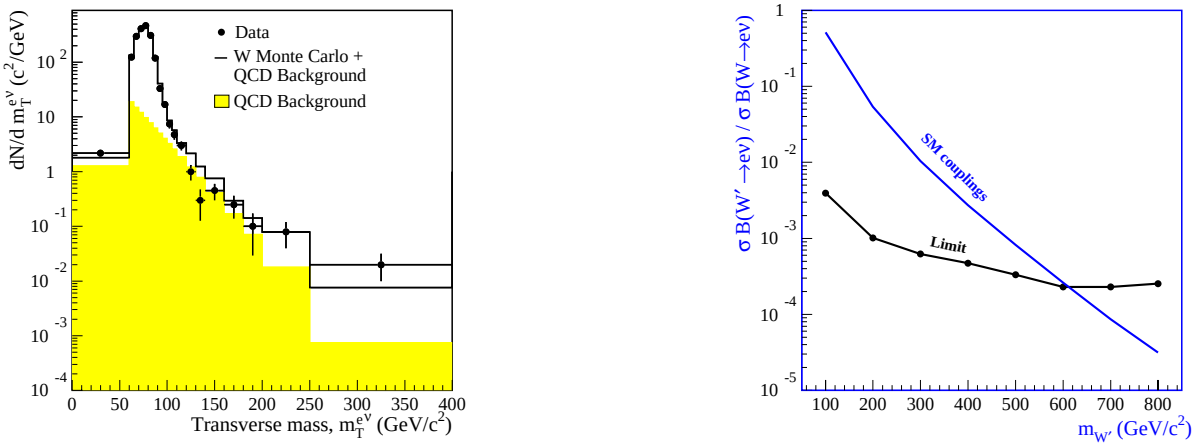

Figure 47: (a) M_T distribution of candidate events in the W' search. Data are shown in points and QCD contribution to background in the shaded area. The sum of W Monte Carlo and the QCD background is shown in histogram. (b) The upper limit on the ratio of the cross section times branching fraction for W'/W boson production at the 95% confidence level. The theoretical prediction for the ratio assuming SM couplings is also shown.

leptons as the SM W boson is excluded at the 95% confidence level for $m_{W'} < 610$ GeV/c^2 assuming that the neutrinos produced in W' decay are stable and have a mass significantly less than $m_{W'}$.

In contrast to the W' search, new final states are possible for the decay of a right-handed W boson (W_R) into a charged lepton and a massive right-handed neutrino (N). It is assumed that the neutrino decays into a charged lepton and a virtual W_R when there is no mixing between the W and W' eigenstates, or into a charged lepton and W boson (virtual or on-shell depending on the mass of the neutrino) in the case of maximum mixing. This analysis examines decays in which the charged lepton is an electron and the gauge boson which results from the decay of the massive neutrino decays into a quark-anti-quark pair. The topology of the final state will depend on the mass of the neutrino. When the neutrino is relatively heavy, the decay products of the W_R boson and N are relatively well separated, resulting in final states with two electrons and two jets. This case is addressed with an event counting analysis. When the neutrino is lighter, the electron from the neutrino decay is not well separated from the jets. In this case, the Jacobian shape of the electron E_T from the two body decay of the W_R boson and the lack of $\not\!\!E_T$ in the W_R signature are used in a fitting analysis.

For the counting analysis, two events pass the selection cuts in the combined 1992-1995 data sample. Backgrounds to this signal include multijet production with two jets misidentified as electrons, Z, γ+jets production, $t\bar{t}$ and WW production. The total background estimate for this search is 3.61 ± 0.60 events.

In the shape fitting analysis, a simultaneous fit was made to the distributions of the transverse mass and the electron E_T. The presence of $W_R \rightarrow eN_R$ events would be evident from an excess in a few consecutive bins of the electron E_T distribution. No such excess is

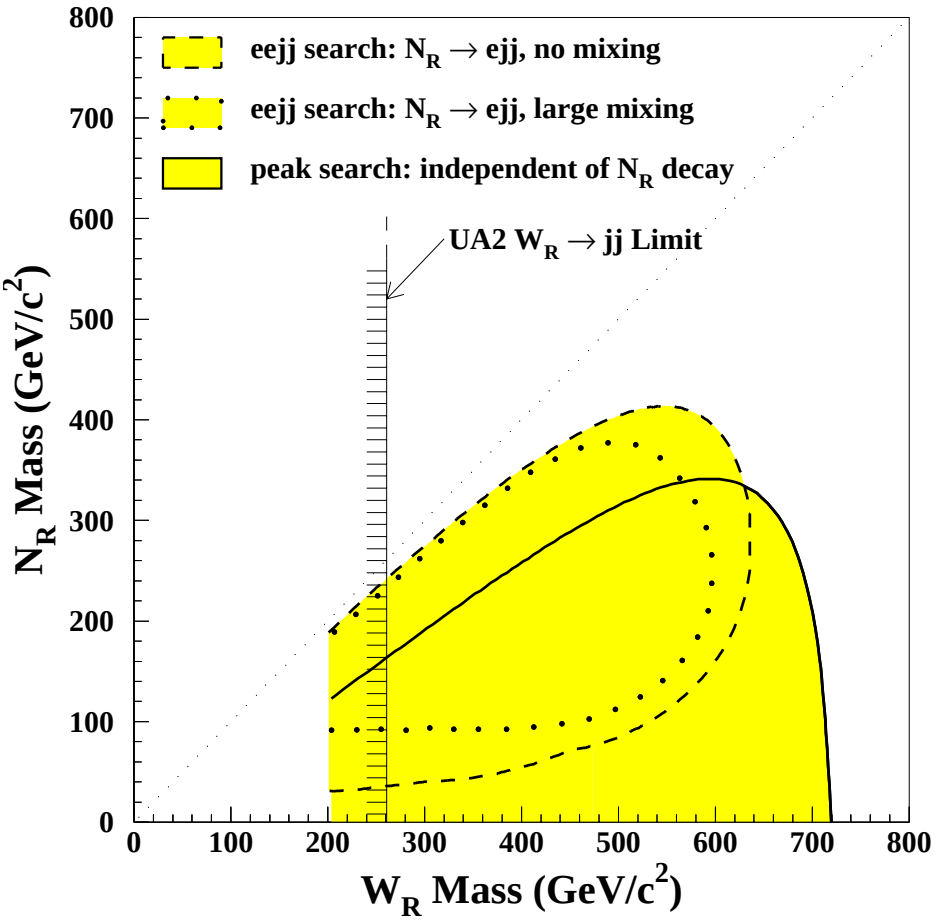

Figure 48: Exclusion contour in the plane of neutrino mass vs. W_R boson mass for combined shape and counting analysis and for minimum and maximum values of mixing between the left- and right-handed bosons.

seen.

Given the lack of an excess above backgrounds, 95% CL upper limits can be set on the cross section times branching ratio for each search. In Fig. 48 the limits from both searches are shown as exclusion contours in the m_{N_R}–m_{W_R} plane, where two contours are drawn for the $eejj$ search: one corresponding the case of no mixing between the W_R and W, and the other for the case of large mixing. The mass limit on W_R, for the case where $N_R = 0$ is also a limit on W' of $m_{W'}$ of 720 GeV. This is an improvement on the search result mentioned above because this analysis includes both data runs.

We have also searched for Z' bosons in the decay channel, $Z' \rightarrow ee$, using the 1992–93 data. The invariant mass spectrum of the data is shown in Fig. 49(a) compared to the sum of Z and Drell-Yan Monte Carlo and QCD dijet background modeled from data. The agreement between data and the simulated prediction is quite good. For $M_{ee} > 140$ GeV/c^2, 12 events are observed. The expected background to Z' from Z/Drell-Yan and dijet events is 8.4 ± 0.4 events. For $M_{ee} > 250$ GeV/c^2, 1 event is observed, and 1.4 ± 0.1 events are expected.

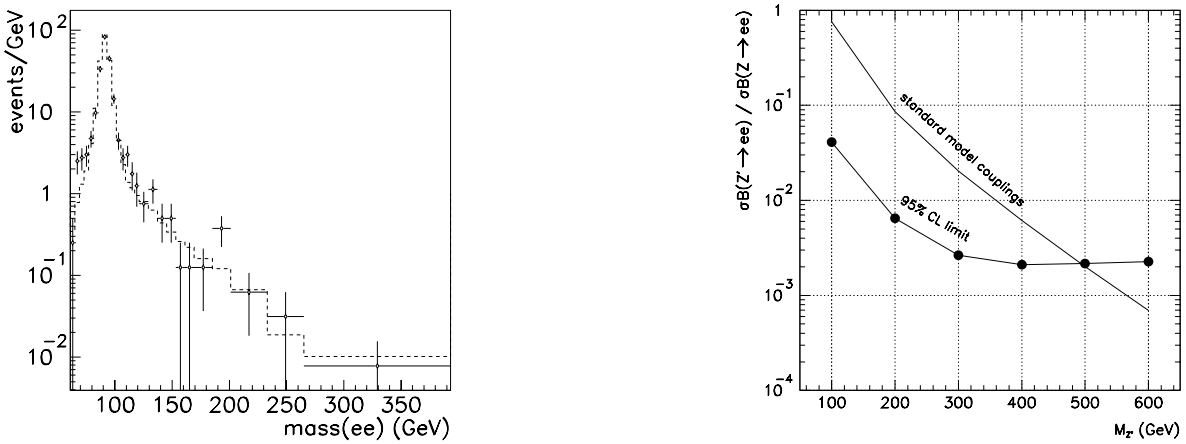

Figure 49: (a) Invariant mass(ee) distribution. Observed dielectron events (discrete points) are compared to the combined Z/Drell-Yan Monte Carlo and dijet background. (b) The 95% CL upper limit on the ratio of the cross section times branching fraction for Z'/Z boson production. The theoretical prediction for the ratio assuming SM couplings is also shown.

The upper limit on the cross section times branching fraction for the process $p\bar{p} \rightarrow Z' \rightarrow ee$ is determined using binned likelihood with Poisson statistics. The 95% CL is plotted as a function of $m_{Z'}$ in Fig. 49(b) together with the theory curve. The theory assumes a Z' with SM couplings to quarks and leptons. There is an uncertainty in the theory of 3% due to choice of pdf's. A Z' from this model is excluded for $m_{Z'} < 490$ GeV/c^2 at the 95% confidence level.

5.3 Fourth Generation Fermions

While the LEP and SLAC experiments have measured the number of light neutrino generations as three, there is still interest in searching directly for evidence of a fourth generation of quarks or leptons, possibly having a heavy neutrino ($m_\nu > 45$ GeV/c^2). DØ has looked for both a fourth generation d-type quark (b') and a fourth generation heavy neutrino.

Standard sequential fourth generation quarks (b', t') are pair produced by the strong interaction with the same cross section, for a given mass, as the bottom or top quarks. Standard model weak decays of either quark can proceed via charged current (CC) or loop-induced flavor changing neutral currents (FCNC). In fact, if the b' is sufficiently light ($m_{b'} < m_t$) FCNC decay modes can predominate. These decay modes are generally to a b quark and a gauge boson or fermion pair. The DØ search has concentrated on the following final states: $b'\bar{b}' \rightarrow \gamma +$ 3 jets $+\mu$-tag and $b'\bar{b}' \rightarrow 2\gamma + 2$ jets.

A fourth generation neutrino could be massive and could mix with other generations in analogy to the quark sector. Assuming that the fourth generation neutrino is lighter than its charged lepton partner, the fourth generation neutrino would decay into a lepton (e, μ, or τ) and W boson. Production of the fourth generation neutrino would proceed via $p\bar{p} \rightarrow W^* \rightarrow l\nu_4$, where $l = e, \mu, \tau$. Thus trilepton final state signatures are possible. The data

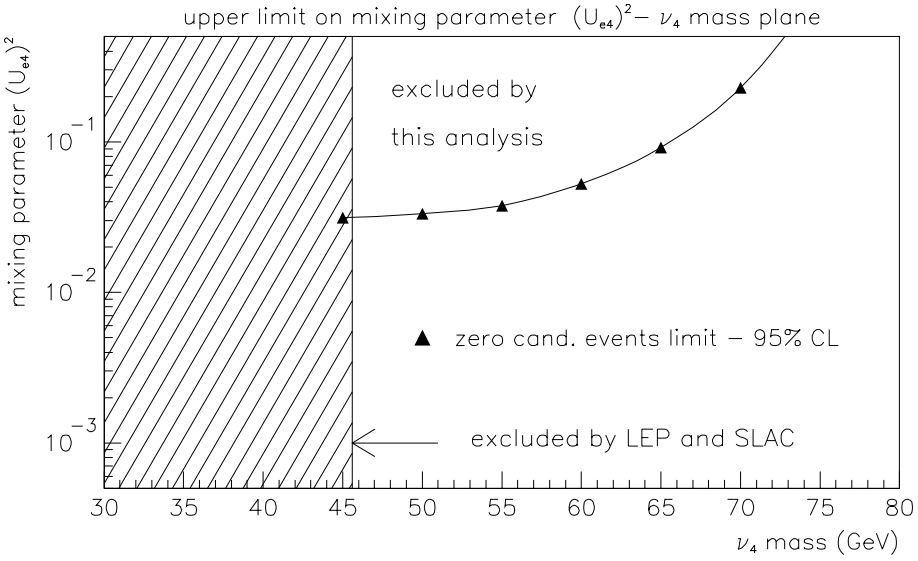

Figure 50: Exclusion contour in the plane of $|U_{e4}|^2$–m_{ν_4} plane for the fourth generation neutrino search.

sample for these final states is the same as for the gaugino trilepton search described earlier. The DØ search has concentrated on $e\nu_4 \rightarrow eee+\not\!\!E_T$ and $ee\mu+\not\!\!E_T$. The resulting limit, shown in Fig. 50, depends on the strength of the ν_1–ν_4 mixing, given by the appropriate element of the unitary mixing matrix U_{ij}.

5.4 Leptoquarks

Exotic particles called leptoquarks appear in many of the theoretical models proposed to go beyond the standard model. A leptoquark carries both lepton quantum numbers and quark quantum numbers (fractional charge, lepton number, baryon number, and color). They would exist as elementary objects in unified theories with large gauge groups, for example E(6) theories and as composite objects in composite and technicolor models. At the HERA *ep* collider, which is an obvious place to search for leptoquarks, the production cross section depends on the unknown coupling of the leptoquark to ordinary quarks and leptons. However, since the leptoquarks carry color, they could be pair-produced in strong interactions at hadron colliders, *independently* of their unknown Yukawa coupling, and their charged lepton decays would produce a distinctive signal (a peak in the lepton-jet invariant mass spectrum). Their decays to neutrinos result in events with high missing transverse energy, which may also be identifiable above background in collider detectors. Due to the constraint imposed by agreement with low-energy phenomena, the different leptoquark generations do not mix. Thus we expect pair-production of the same generation leptoquarks with each leptoquark decaying only to a lepton + quark (with branching ratio β) or into a ν plus

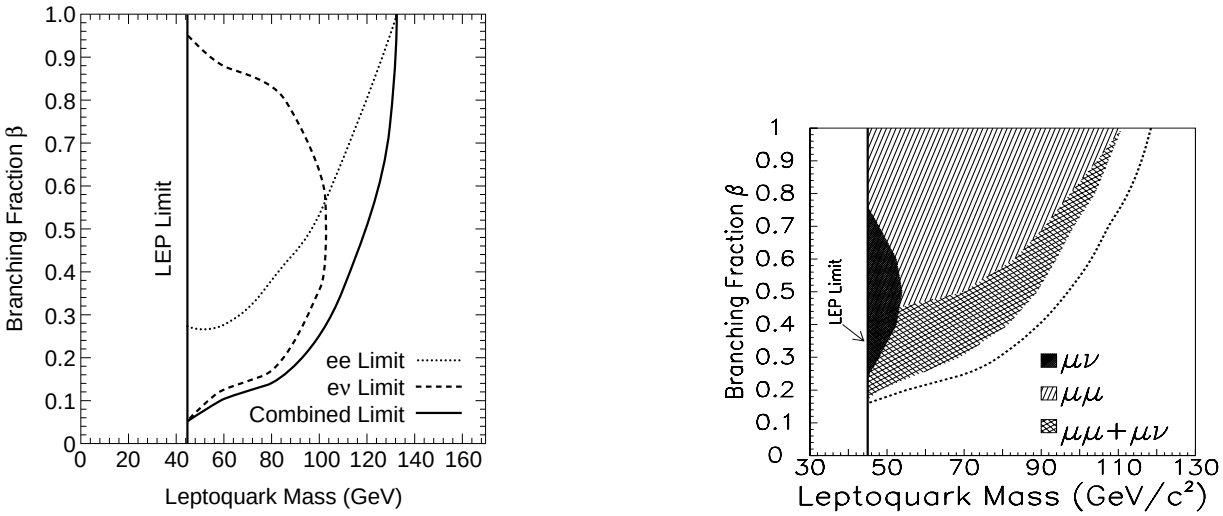

Figure 51: (a) The 95% CL lower limit on the first generation leptoquark mass as a function of β. (b) The 95% CL lower limit on the mass of the second generation leptoquark. In each case the limit from the dilepton, single lepton, and combined search is shown.

quark (with branching ratio $1-\beta$), where the leptons and quarks are all from the same generation. DØ has published search limits on both first and second generation leptoquarks, by searching for final states of electrons plus jets and muons plus jets.

No candidates were found in either the electron or the muon channels. Based on this analysis, we set 95% CL upper limits on the cross section times branching ratio for first and second generation leptoquarks. These limits are shown in Fig. 51.

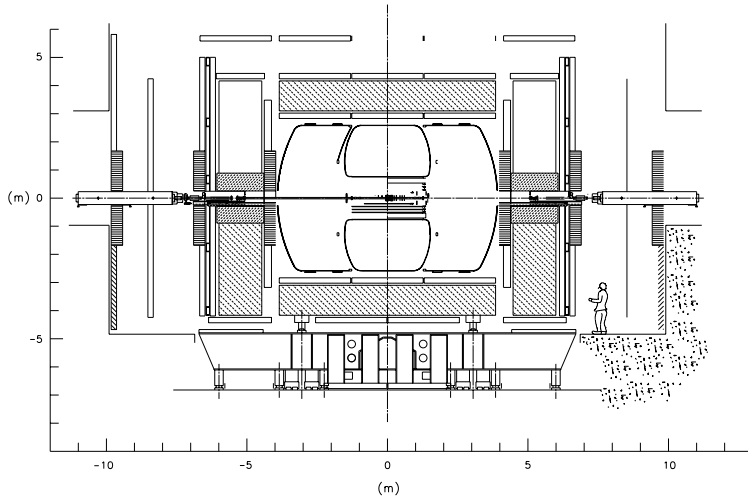
5
(m) 0
-5
-10
-5
0
5
10
(m)